Available online at www.sciencedirect.com

ScienceDirect

Deep-Sea Research I 54 (2007) 1593–1618

DEEP-SEA RESEARCH PART I

www.elsevier.com/locate/dsri

Modelling the effect of cell-size-dependent nutrient uptake and exudation on phytoplankton size spectra

Iris Kriest*, Andreas Oschlies

Leibniz-Institute of Marine Sciences at Kiel University (IFM-GEOMAR), Kiel, Germany

Received 25 July 2006; received in revised form 20 April 2007; accepted 24 April 2007
Available online 22 May 2007

Abstract

The effect of phytoplankton cell size on the variation of nutrient uptake and exudation rates is examined: we first present an overview of the relationship between the variation of the growth and loss parameters and cell size. We then investigate the effect of cell-size-dependent parameters on the development of an entire phytoplankton community by means of a numerical, vertically resolved nutrient–phytoplankton model. The model represents phytoplankton size distributions in three different ways, namely one configuration with explicit representation of 14 size classes, one configuration with constant-slope power-law spectral representation, and one configuration with variable-slope power-law spectral representation. The size-dependent configurations are further compared to a size-independent configuration. Consistent with theory, the explicit and variable-slope spectral model simulations predict increased importance of larger cells, or "flat" size distribution under conditions of low light and high nutrients, while smaller cells ("steep" size distributions) may dominate in oligotrophic, well-lit regimes. In some situations the variable-slope spectral model seems to be sufficient to reflect the phytoplankton size distribution; however, especially in the deep phytoplankton maximum a unimodal rather than power-law spectral description might be more appropriate to reproduce results of the explicit 14-size-class model. The assumption of a fixed spectral slope, according to which larger size classes gain importance especially during bloom periods, is not consistent with the underlying theory, and does not agree with the results of the size-discrete model. The comparison of model predictions with variations of phytoplankton size distribution observed in the field is hampered by the sparsity of data, especially for the winter season. A half-saturation constant that represents the nutrient uptake of the entire phytoplankton community (K^*) compares well to published values.

Keywords: Phytoplankton; Nutrient uptake; Exudation; Cell size; Size spectra; Model

1. Introduction

Current marine ecosystem models that attempt to describe life's action on marine biogeochemical cycles typically partition the marine ecosystem into a handful of compartments, such as phytoplankton, zooplankton, or detritus. Using mass conservation as an underlying concept, the individual compartments simulate stocks of atoms of one or more key element(s) under consideration. The modelled processes, e.g., primary production, grazing, or exudation all describe the transfer of atoms among the different compartments. To date, a solid theoretical

*Corresponding author. Tel.: +49 431 600 4027; fax: +49 431 600 1515.
E-mail addresses: ikriest@ifm-geomar.de (I. Kriest), aoschlies@ifm-geomar.de (A. Oschlies).

0967-0637/$ - see front matter © 2007 Elsevier Ltd. All rights reserved.
doi:10.1016/j.dsr.2007.04.017

framework for the description of such fluxes does not exist nor does a complete and consistent mapping of the real ecosystem onto a small number of model compartments. In the absence of any known ecological equivalent of the Navier–Stokes equations, which give firm guidance to the construction of physical ocean circulation models, the particular choice of the ecosystem model structure is generally based on subjective elements and often influenced by operational measurement protocols, historical paradigms, or taxonomic nomenclature rather than some *a priori* knowledge of physical or biochemical mechanisms.

Despite the considerable reliance on subjective elements, current models have often shown remarkable success in simulating many observed properties and dynamics of marine ecosystems, at least in a qualitative sense. Quantitatively, success or failure of a particular model structure may be judged in terms of model-data misfits. While defining an "objective" misfit function is not straightforward and will always include some subjective elements, its combination with data-assimilation methods can yield a performance measure of a given model that does not depend on subjective tuning (or the absence thereof) of the often poorly known parameter values. This approach has, so far, been applied predominantly to Nutrient–Phytoplankton–Zooplankton–Detritus (NPZD) type models which contain about 10–30 parameters. Models have been fitted to data sets at individual time-series and process-study sites (Matear, 1995; Fasham and Evans, 1995; Prunet et al., 1996a, b; Hurtt and Armstrong, 1996; Spitz et al., 1998, 2001; Fennel et al., 2001; Schartau et al., 2001; Dadou et al., 2004; Friedrichs et al., 2006) and also to data at different locations simultaneously (Hurtt and Armstrong, 1999; Schartau and Oschlies, 2003a, b).

Common to all of the above assimilation studies is that at most 10–15 ecological model parameters (or linear combinations thereof) can be constrained by the available observations. Even for the relatively simple NPZD-type models there are always a few parameters that cannot be constrained, suggesting that models with fewer parameters should be able to achieve a similarly good (or bad) fit to the observations. At the same time, the degree to which the models can quantitatively reproduce the observations is, in general, not satisfactory, i.e., model-data misfits tend to be much larger than the prior observational error estimates. While this may to some extent be explained by errors in the description of the physical environment (Friedrichs et al., 2006), it nevertheless suggests that the employed NPZD-type models may have inadequate structures and may lack important elements of yet unknown ecological rules of marine ecosystems.

Similar conclusions may be drawn from the results of a regional data-assimilation study by Losa et al. (2004), which needed spatially varying biological parameters in order to reproduce remotely sensed pigment concentrations in a regional model of the North Atlantic. Analogously, Harrison et al. (1996) observed spatially varying half-saturation "constants" for nitrate uptake from 10^{-3} to $1.32\,\mathrm{mmol\,N\,m^{-3}}$ in the North Atlantic, which increased approximately exponentially with increasing ambient nitrate concentration. For many purposes like simulating different climate conditions, prescribed model parameters that vary spatially may not be appropriate. Attempts to resolve this issue include strategies to make models more complex, in particular by adding several distinct phytoplankton groups with specific parameters that are constant for each group (e.g., Gregg et al., 2003). The drawback of this approach is the increase of the number of parameters which, for present observational data sets, are difficult to constrain. Although additional degrees of freedom can help to improve a model's fit to individual data sets, data-assimilation studies could not yet demonstrate that such models lead to significant improvements in predictive power, i.e., when evaluated against observations not already used for model calibration (Friedrichs et al., 2006).

In the present study, we follow an alternative strategy and ask to what extent we can use theoretical considerations of some of the processes that cause variations in the parameters assumed constant in NPZD-type models. Focussing on the phytoplankton compartment of ecosystem models we will, in this paper, begin with a simple nutrient–phytoplankton model under idealized forcing. Our emphasis in this paper is on variations in nutrient uptake and loss processes of phytoplankton, and our hypothesis is that these variations can be related to differences in cell size. The model's performance with respect to reproducing observed trends in the variation of half-saturation constant is considered as a qualitative indicator about the validity of the assumptions made. We believe that more extensive use of mechanistic rules will eventually help to better understand the underlying ecological processes and to make more reliable

predictions for different future scenarios. Such a mechanistic understanding is particularly important for more reliably predicting what will happen under, for example, pCO_2 and alkalinity levels exceeding those experienced over the past few hundred thousand years, i.e., conditions not reflected in our data bases used to fit marine ecosystem models.

Subsequent studies will look at more complex models and investigate how the inclusion of zooplankton and dissolved-organic-matter processes affect model performance. The present paper is organized as follows: In Section 2 we describe how cell size may theoretically affect transport processes across cell membranes. In Section 3 we describe various methods to account for size distributions in a numerical model, and Section 4 presents results of one explicitly and two implicitly size-structured nutrient–phytoplankton models in a one-dimensional setting corresponding to an annual cycle at a North Atlantic spring bloom site.

2. Theoretical considerations about size-dependent processes

2.1. Growth: the formulation by Aksnes and Egge (1991)

Aksnes and Egge (1991) related the nutrient uptake by marine phytoplankton to the number of uptake sites per unit cell surface area (a, [m^{-2}]), the size of a particular site (A_s, [m^2]), and the handling time at a particular site per unit ion (in our case, NO_3^-; h [d mmol^{-1}]). Assuming that the number of uptake sites n is linearly related to the cell surface area and that rate processes are not limited by light (this assumption will be relaxed below by introducing a separate light limitation term), the (cell) biomass-normalized nitrate-uptake rate ($V_N(d)$, [d^{-1}]) becomes

$$V_N(d) = \pi d^2 \frac{a}{b(d)\,h} \frac{NO_3}{\frac{d}{2\,h\,A_s\,D} + NO_3}. \quad (1)$$

Here, D is the molecular diffusivity of the nutrient (here NO_3) in the water surrounding the cell [$m^2\,d^{-1}$], NO_3 is the ambient nitrate concentration [mmol N m^{-3}], d is the diameter of an idealized spherical cell [m], and $b(d)$ is the cell biomass [mmol N]. In this approach it is assumed that the cells are not able to distort the medium (i.e., that the sinking velocity is much smaller than the diffusion coefficient divided by the radius, see Aksnes and Egge, 1991), so that the mass transfer toward the cell is determined by molecular diffusivity alone. Eq. (1) can be converted into the well-known "Monod-type" function

$$V_N = \frac{\mu\,NO_3}{K + NO_3} \quad (2)$$

with maximum light-saturated growth rate μ[d^{-1}] and half-saturation constant K [mmol N m^{-3}], by making both μ and K explicit functions of the cell diameter d. The maximum light-saturated growth rate therefore is

$$\mu(d) = \pi d^2 \frac{a}{b(d)h}, \quad (3)$$

and the half-saturation "constant" becomes

$$K(d) = \frac{d}{2hA_sD}. \quad (4)$$

Little quantitative information is available on the microscopic parameters a, A_s, and h, but we have some empirical information about macroscopic parameters such as the minimum half-saturation "constant" K and the maximum light-saturated growth rate μ. Moreover, we have defined A_s and h as site-specific, i.e., we assume that they do not vary with cell size. Assuming some minimum cell size (e.g., $d_1 = 0.2\,\mu m = 2 \times 10^{-7}$ m), we can use estimates of the corresponding half-saturation constant $K_1 = K(d_1 = 0.2\,\mu m)$ (e.g., 0.005 mmol N m^{-3}) and similarly for $\mu_1 = \mu(d_1 = 0.2\,\mu m) = 2\,d^{-1}$. Then

$$K(d) = K_1 \frac{d}{d_1}, \quad (5)$$

i.e., the half-saturation "constant" increases linearly with increasing size, with the smallest cells (of diameter d_1) having the smallest half-saturation constant K_1. The expression for the maximum light-saturated growth rate can be simplified by assuming that biomass of a cell, b, depends on its diameter according to a power law: $b(d) = Cd^{\zeta}$ (Mullin et al., 1966):

$$\mu(d) = \mu_1 \left(\frac{d}{d_1}\right)^{2-\zeta}, \quad (6)$$

where μ_1, the maximum possible growth rate for the smallest cells of diameter d_1, may be as high as ≈ 2–$3\,d^{-1}$ (Banse, 1976; Chisholm, 1992; Tang, 1995; Montagnes and Franklin, 2001).

Via the exponent ζ, the maximum light-saturated growth rate depends on the relationship between cell carbon (or nitrogen) content and cell diameter.

For marine planktonic algae ζ is found to lie between ≈ 2.1 (Strathmann, 1967, for diatoms) and ≈ 3 (Montagnes et al., 1994, mixed phytoplankton assemblage), with carbon-to-volume relationships of diatoms seeming to have lower exponents than those of flagellates (Menden-Deuer and Lessard, 2000). Accordingly, the decrease of growth rate with size might be expected to be less pronounced when diatoms are considered than when the analysis is based on flagellates.

While the present exploratory study does not attempt to distinguish between different species and will employ a single exponent ζ for all phytoplankton, possible future refinements of the model may include different carbon-to-volume relationships (and possibly different values of μ_1 and K_1) for different phytoplankton species or functional groups. By inserting the size-dependent expressions (5) and (6) into (2) the size-dependent light-saturated nitrate uptake by phytoplankton becomes

$$V_N(d) = \frac{\mu(d)\,NO_3}{K(d) + NO_3} = \frac{\mu_1 \left(\frac{d}{d_1}\right)^{2-\zeta} NO_3}{K_1 \frac{d}{d_1} + NO_3}. \quad (7)$$

Note that for the special case of $\zeta = 2$ Eq. (7) is equivalent to the formulation for light-saturated nutrient uptake used by Hurtt and Armstrong (1999) when their parameter β'_k is set to 1.

To account for the effect of light on phytoplankton growth, we now assume a multiplicative co-limitation by light and nutrients of which the light limitation V_I is given by the Smith (1936) formula, normalized by maximum light-saturated growth rate, μ:

$$V_I = \frac{\alpha I}{\sqrt{\mu^2 + \alpha^2 I^2}} = \frac{\frac{I}{I_k}}{\sqrt{1 + \left(\frac{I}{I_k}\right)^2}} \quad \text{where } I_k = \frac{\mu}{\alpha}. \quad (8)$$

α is the initial slope of the P–I curve and μ is the maximum growth rate under light- and nutrient-replete conditions. As stated above, $\mu = \mu(d)$ depends on cell size.

Measurements taken from various diatom cultures under nutrient-replete conditions and varying light intensities suggest that the initial slope α depends also on cell size and, in fact, shows a decrease of α with increasing cell size in a similar way as the maximum growth rate (Taguchi, 1976). We here assume that the initial slope α follows the same functional relationship with cell size as the maximum growth rate μ:

$$\alpha(d) = \alpha_1 \left(\frac{d}{d_1}\right)^{2-\zeta}. \quad (9)$$

For the observed range of $2 < \zeta < 3$ this corresponds to $\alpha(d)$ decreasing with increasing cell size. Theoretical models suggest such a decrease as a result of the package effect, which is a consequence of enhanced self-shading of chloroplasts within larger cells (Geider et al., 1986; Fujiki and Taguchi, 2002).

As a consequence, I_k in Eq. (8) does not depend on size and is given by $I_k = \mu_1/\alpha_1$. Light limitation is then a function of light alone:

$$V_I = \frac{I \frac{\alpha_1}{\mu_1}}{\sqrt{1 + \left(\frac{\alpha_1}{\mu_1}\right)^2 I^2}}. \quad (10)$$

Combining Eqs. (7) and (10) by a multiplicative approach, the realized nutrient- and light-limited growth becomes

$$V(I, NO_3, d) = V_I V_N(d) = \frac{I \frac{\alpha_1}{\mu_1} \quad \mu_1 \left(\frac{d}{d_1}\right)^{2-\zeta} NO_3}{\sqrt{1 + \left(\frac{\alpha_1}{\mu_1}\right)^2 I^2} \quad K_1 \frac{d}{d_1} + NO_3}. \quad (11)$$

The above expression describes how nutrient uptake depends on light, ambient nutrient concentration, and cell size. Note that for any given nitrate and light condition (and for any ζ within the observed range $2 < \zeta < 3$), nutrient uptake decreases with increasing cell size d. One may wonder why large cells exist at all. There are at least three strategic advantages large cells may have. All of them are related to losses a cell might experience:

- Increasing the size (= decreasing the surface: volume ratio) decreases the losses via exudation (= diffusion of organic compounds out of the cells) (Bjørnsen, 1988).
- Larger cells may have more efficient storage mechanisms for photosynthetic products (Raven and Kübler, 2002), which may help them to persist even through (limited) periods of oligotrophy.

- Increasing size helps phytoplankton to avoid being grazed by microzooplankton. Larger zooplankton (e.g., copepods) grow more slowly and often have longer life cycles, which helps phytoplankton to escape the grazing.

In the following we investigate exudation as one size-sensitive process that may explain the observed existence of large cells.

2.2. Exudation: the formulation by Bjørnsen (1988)

In contrast to other studies which assumed exudation to be related to production, Bjørnsen (1988) postulated that the loss of organic compounds from phytoplankton cells should be related to biomass. Assuming that the concentration of low-molecular-weight organic matter in the surrounding water is low compared to that in cells and that exudation is a passive process, the biomass-specific loss according to Bjørnsen (1988) is

$$\lambda(d) = P \cdot \mathrm{LMW} \cdot 6 \cdot d^{-1} = \lambda_1 \left(\frac{d}{d_1}\right)^{-1}, \qquad (12)$$

where P is the permeability of the cell membrane, LMW is the fraction of low-molecular-weight compounds of total cell biomass, and d is the cell diameter. Thus, loss of organic matter decreases with increasing size. For example, for a cell with $d = 2\,\mu\mathrm{m}$, a permeability $P \approx 10^{-9}\,\mathrm{cm\,s^{-1}}$ for amino acids, and LMW content = 10% (the values used by Bjørnsen), losses are $\approx 0.25\,\mathrm{d^{-1}}$. By contrast, for a cell with $d = 0.2\,\mu\mathrm{m}$ the same calculation results in a loss-rate of about $2.5\,\mathrm{d^{-1}}$, which seems far too high. Given that the permeability depends strongly on the molecule size and is about an order of magnitude lower ($10^{-10}\,\mathrm{cm\,s^{-1}}$) for glucose, we set $\lambda_1 = 0.2\,\mathrm{d^{-1}}$ as an approximation for cells with $d = 0.2\,\mu\mathrm{m}$.

2.3. Combined effects of both approaches

In the following, we investigate the results of a combination of the above approaches that relate nutrient uptake and loss-rates to cell size. Based on these relations, we aim to identify environmental conditions that will favor or discriminate against certain phytoplankton size classes. For the smallest size class represented ($d_1 = 0.2\,\mu\mathrm{m}$), we set the maximum growth rate to $\mu_1 = 2\,\mathrm{d^{-1}}$, the exudation rate to $\lambda_1 = 0.2\,\mathrm{d^{-1}}$, the half-saturation constant $K_1 = 0.005\,\mathrm{mmol\,NO_3\,m^{-3}}$, and the initial slope of the P–I curve to $\alpha_1 = 0.05\,\mathrm{d^{-1}}\,(\mathrm{W/m^2})^{-1}$. For the relationship between biomass and cell size we use the empirically determined exponent $\zeta = 2.28$ (Mullin et al., 1966) and, alternatively, $\zeta = 2$ for which the maximum growth rate becomes independent of size.

Fig. 1 shows the combined effect of nutrient and light limitation, and exudation on phytoplankton net growth rates. Because $\zeta = 2.28$ implies decreasing maximum growth rate with increasing cell size (left panels of Fig. 1), net growth rate decreases monotonously with increasing cell size at high light levels. (Note that we assume the net growth rate to be equivalent to net nutrient uptake rate.) At low light intensities, however, large cell size is an advantage because it allows losses via exudation to be reduced to a rate that may still be balanced by nutrient uptake under eutrophic conditions. For the chosen parameter values this is the case for cell sizes larger than about $0.4\,\mu\mathrm{m}$.

For size-independent maximum growth rates ($\zeta = 2$) and medium to high nutrient concentrations, net growth rates show a maximum at cell sizes $>0.2\,\mu\mathrm{m}$ even at high light intensities (upper right panel of Fig. 1, dotted and dashed lines). As can also be determined analytically, the optimum cell size increases with decreasing light and increasing nutrients. This is qualitatively similar to the trend found for $\zeta = 2.28$.

The combination of size-dependent formulations of nutrient uptake and exudation simulates different responses of small and large cells to different environmental conditions: small cells are favored under high-light and low-nutrient conditions, whereas large cells have a relative advantage under low-light and high-nutrient conditions. According to this hypothesis we should expect the dominance (in terms of biomass) of larger cells in temperate regions during spring time or in the nutricline, and smaller cells to dominate under oligotrophic and high-light conditions.

3. Population growth and loss in a size-spectral representation

So far we have considered effects of growth and exudation on single phytoplankton cells of a certain diameter. In this section, we describe how the above representations of size-dependent processes can be combined with simple assumptions about particle size distribution to prepare for the modelling of entire phytoplankton communities. One option to introduce size-dependent nutrient uptake, growth,

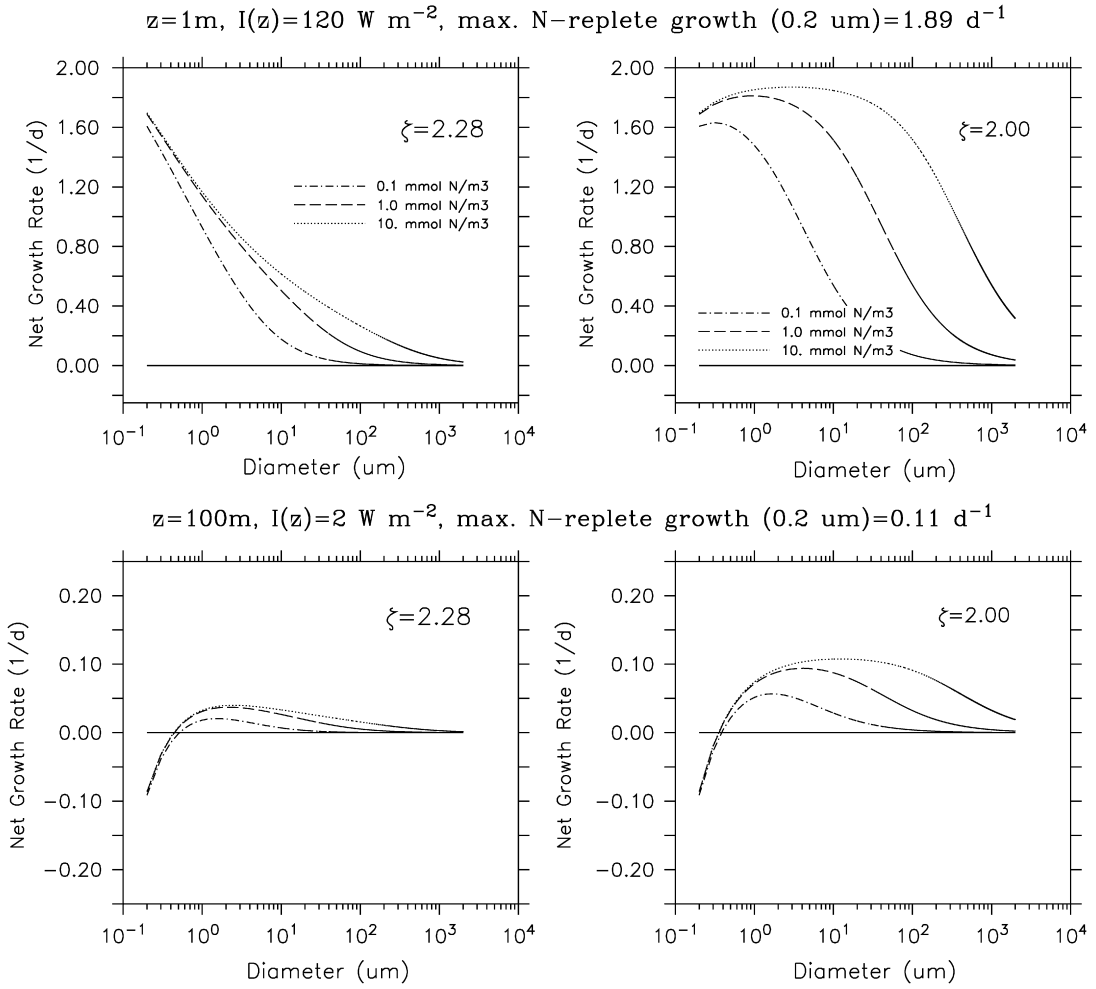

Fig. 1. Net growth rates derived from the combined Aksnes–Bjørnsen model (Eq. (11) minus Eq. (12)), plotted against cell diameter for three different nitrate concentrations (see legend). Left panels: $\zeta = 2.28$. Right panels: $\zeta = 2.00$. Upper panels: $z \approx 1$ m. Lower panels: $z \approx 100$ m. Light intensity at depth z has been calculated according to $I(z) = I_0 \exp(-0.04\, z\, I_0)$ with $I_0 = 125\,\mathrm{W\,m^{-2}}$, i.e., without taking into account self-shading by phytoplankton.

and exudation rates in ecosystem models is to explicitly resolve a large number of different size classes (Baird et al., 2004). Here, we contrast this with a computationally cheaper and more pragmatic approach by assuming that the phytoplankton size distribution can be described by a power law (albeit with temporally and regionally varying parameters). For a given size spectrum, the size-dependent rates can then be integrated over the entire spectrum, yielding effective rates for the whole population.

3.1. Spectra of biomass and particle abundance

Empirical relationships between particle abundance, N, and particle size are often described by a power law

$$n(d) = \frac{\mathrm{d}N}{\mathrm{d}d} = Ad^{-\varepsilon} \tag{13}$$

(e.g., McCave, 1984; Weilenmann et al., 1989), where $N(d)$ is the number of particles per size class d. While the power-law description often seems appropriate when cell size and abundance are plotted on a log–log scale, there is no guarantee that such a relationship precisely fits the size distribution of marine planktonic ecosystems. Other spectral distributions, e.g., a log-normal one as described by Jonasz and Fournier (1996), may turn out to be more appropriate. To keep our model conceptionally simple we assume that the phytoplankton size distribution can be described

by a power law (Eq. (13)). We also assume that the biomass of a particle with diameter d can be described by $b(d) = C\,d^{\zeta}$ (ζ assumed to be constant), so that the normalized mass distribution is given by

$$m(d) = \frac{\mathrm{d}M}{\mathrm{d}d} = ACd^{\zeta-\varepsilon}, \tag{14}$$

where M is the mass per size class d. Here, an exponent $\varepsilon = \zeta + 1$ means that mass is distributed evenly between logarithmically increasing size classes. This type of mass distribution has also been referred to as "flat" (e.g., Rodriguez and Mullin, 1986; Gin et al., 1999).

3.2. Population growth

Combining the size-dependent nutrient uptake (Eq. (11)) with the phytoplankton biomass distribution (Eq. (14)), we can calculate the gain of mass of the entire population, P, due to photosynthesis:

$$\begin{aligned} P(\varepsilon, \mathrm{NO_3}) &= V_I AC \frac{\mu_1}{d_1^{2-\zeta}} \int_{d_1}^{d_L} d^{\zeta-\varepsilon} \frac{\mathrm{NO_3}\,\mathrm{d}d}{d^{\zeta-2}\left(\frac{K_1}{d_1}d + \mathrm{NO_3}\right)} \\ &= V_I A\,\mathrm{NO_3} b_1 \frac{\mu_1}{d_1^2} \int_{d_1}^{d_L} \frac{\mathrm{d}d}{d^{\varepsilon-2}\left(\frac{K_1}{d_1}d + \mathrm{NO_3}\right)}, \end{aligned} \tag{15}$$

where d_1 and b_1 are the diameter and biomass of the smallest cell, respectively. We here refer to the upper boundary of the integral as d_L which can, depending on the convergence properties of the integral considered, either be a finite or an infinite maximum cell size. This integral can be solved analytically for integer exponents n, i.e., for $n = \varepsilon - 2 \geqslant 1$:

$$\begin{aligned} P(n, \mathrm{NO_3}) &= V_I A\,\mathrm{NO_3}\, b_1 \frac{\mu_1}{d_1^2} \int_{d_1}^{d_L} \frac{\mathrm{d}d}{d^n\left(\frac{K_1}{d_1}d + \mathrm{NO_3}\right)} \\ &= -V_I A\,\mathrm{NO_3} b_1 \frac{\mu_1}{d_1^2} \left[\sum_{i=1}^{n-1} \frac{\left(-\frac{K_1}{d_1}\right)^{i-1}}{(n-i)d^{n-i}\mathrm{NO_3^i}} \right. \\ &\quad \left. + \frac{\left(-\frac{K_1}{d_1}\right)^{n-1}}{\mathrm{NO_3^n}} \ln\left(\frac{\frac{K_1}{d_1}d + \mathrm{NO_3}}{d}\right) \right]_{d_1}^{d_L} \end{aligned} \tag{16}$$

By expressing d_L as a multiple of d_1, such that $\frac{d_1}{d_L} = f$, the solution of the integral from d_1 to d_L then becomes:

$$\begin{aligned} P(n, \mathrm{NO_3}) &= V_I A b_1 \frac{\mu_1}{d_1^2} \frac{1}{d_1^{n-1}} \\ &\quad \times \left[\sum_{i=1}^{n-1} \frac{\left(\frac{-K_1}{\mathrm{NO_3}}\right)^{i-1}}{(n-i)} - \sum_{i=1}^{n-1} \frac{\left(\frac{-K_1}{\mathrm{NO_3}}\right)^{i-1} f^{n-i}}{(n-i)} \right. \\ &\quad \left. - \left(\frac{-K_1}{\mathrm{NO_3}}\right)^{n-1} \ln\left(\frac{K_1 + \mathrm{NO_3} f}{K_1 + \mathrm{NO_3}}\right) \right]. \end{aligned} \tag{17}$$

3.3. Population exudation

The exudation term of the phytoplankton biomass equation can be computed in close analogy to the production term. The total population loss, L, is given by the integral over the product of Eqs. (12) and (14).

$$L(\varepsilon) = AC\lambda_1 d_1 \int_{d_1}^{d_L} d^{\zeta-\varepsilon-1}\,\mathrm{d}d. \tag{18}$$

3.4. Practical considerations

The effect of size-dependent nutrient uptake on the entire phytoplankton population may be investigated under three different assumptions about changes in a population's size structure. The first assumption follows Hurtt and Armstrong (1999) and assumes a *constant spectral exponent* of $\zeta - \varepsilon = -1$ and a constant coefficient A, but a varying upper boundary d_L, which is diagnosed at every time step from phytoplankton biomass. The second assumption is based on the approach used by Kriest and Evans (1999) to describe marine snow aggregates. It assumes varying size distribution parameters ε and A ("variable spectral exponent"), but a constant upper boundary for maximum cell size, d_L. The approach solves for the two unknown parameters ε and A at each time from the solution of two prognostic equations: a standard one for the total biomass of the phytoplankton population, and a second one for the total number of phytoplankton cells per volume. The third approach accounts for possible peaks of biomass in the size spectrum by resolving explicitly a (limited) number of size classes.

3.4.1. Size-dependent growth and exudation with constant spectral exponent

Growth. Hurtt and Armstrong (1999) assumed a fixed exponent of $\zeta-\varepsilon=-1$ (a "flat" mass spectrum) and a constant factor A for the distribution of mass versus diameter (Eq. (14)), but estimated the upper boundary for integration d_L from the total phytoplankton mass concentration. In the context developed above, for $\zeta=2$ and hence $\varepsilon=3$ and $n=1$, only the logarithmic evaluation of Eq. (17) remains:

$$P(n=1,\mathrm{NO_3}) = V_I A b_1 \frac{\mu_1}{d_1^2} \ln\left(\frac{K_1+\mathrm{NO_3}}{K_1+\mathrm{NO_3} f}\right) \tag{19}$$

with $f=d_1/d_L$ as defined above. The integral for Eq. (14) over a finite range $[d_1,d_L]$ is $\mathrm{PHY}=AC\ \ln(\frac{d_L}{d_1})$, and Eq. (19) becomes

$$P(n=1,\mathrm{NO_3}) = V_I A C \mu_1 \ln\left(\frac{K_1+\mathrm{NO_3}}{K_1+\mathrm{NO_3}\,\mathrm{e}^{-\mathrm{PHY}/AC}}\right), \tag{20}$$

which is equivalent to the Hurtt and Armstrong (1999) derivation of the phytoplankton growth rate (their equation (11)) for $\beta'_k=1$. Note that if we, for whatever reason, disregard any size dependence of μ on d, then this even holds for $\zeta\neq 2$ as long as $\zeta-\varepsilon=-1$.

Exudation. In the case of the Hurtt and Armstrong (1999) framework (for $\zeta-\varepsilon=-1$), the appropriate term for the size-dependent exudation in the biomass equation simplifies to

$$\begin{aligned} L(\varepsilon=3) &= AC\lambda_1 d_1 \int_{d_1}^{d_L} d^{-2}\,\mathrm{d}d \\ &= AC\lambda_1(1-\mathrm{e}^{-\mathrm{PHY}/AC}), \end{aligned} \tag{21}$$

where we have again used the fact that for $\zeta-\varepsilon=-1$ the solution of equation (14) over a finite range $[d_1,d_L]$ is $PHY=A\,C\ln(\frac{d_L}{d_1})$.

3.4.2. Size-dependent growth with variable spectral exponent

Growth. We now relax the constraint of a "flat" mass spectrum and allow for arbitrary spectral exponents. To solve for the temporally and spatially varying coefficient A and exponent ε of the power spectrum, we follow the approach of Kriest and Evans (1999). In that study the size distribution of phytoplankton aggregates was parameterized by a power law and variations of A and ε were diagnosed from the variation of particle number and mass. Let $b_1=Cd_1^{\zeta}$ again denote the biomass of the smallest cell (of diameter d_1). Then the total phytoplankton biomass per volume is given by

$$\begin{aligned} \mathrm{PHY} &= AC\int_{d_1}^{d_L} d^{\zeta-\varepsilon}\,\mathrm{d}d \\ &= Ab_1\frac{d_1^{1-\varepsilon}}{\varepsilon-1-\zeta}(1-f^{\varepsilon-\zeta-1}), \end{aligned} \tag{22}$$

where, as before, $f=d_1/d_L$ is the ratio of smallest to largest cell diameter. Accordingly, the total number of cells is

$$\mathrm{NOS} = A\int_{d_1}^{d_L} d^{-\varepsilon}\,\mathrm{d}d = A\frac{d_1^{1-\varepsilon}}{\varepsilon-1}(1-f^{\varepsilon-1}). \tag{23}$$

Once the total biomass PHY and total cell number NOS are known, the exponent ε of the normalized concentration spectrum (13) can be computed numerically. While numerical evaluation of ε can be quite time consuming, ε can be computed analytically for the special case of infinite upper boundaries of the phytoplankton size distribution ($d_L\to\infty, f\to 0$, as in Kriest and Evans (1999)) as

$$\varepsilon = \frac{(\zeta+1)\,\mathrm{PHY}-b_1\,\mathrm{NOS}}{\mathrm{PHY}-b_1\mathrm{NOS}}. \tag{24}$$

The above relation implies that for any initial particle distribution that meets the $\varepsilon>\zeta+1$ condition (required for convergence of the biomass integral for $d_L\to\infty$), the slope of the size spectrum can only approach $\zeta+1$, but can never become smaller. To minimize computational costs we will consider the phytoplankton size range to be infinite and evaluate ε according to Eq. (24).

The more general case of non-integer exponents ($\varepsilon-2$ in Eq. (15)) can in principle be solved numerically for a given size range d_1 to d_L. Again, this can be computationally expensive. To achieve analytical solutions that rely on integer exponents, we assume that the size distribution as described by Eqs. (13) and (14) can be replaced by a polynomial:

$$n(d) = A_1 d^{-(\varepsilon_i+1)} + A_2 d^{-\varepsilon_i} = A d^{-\varepsilon} \tag{25}$$

and

$$m(d) = A_1 C d^{\zeta-(\varepsilon_i+1)} + A_2 C d^{\zeta-\varepsilon_i} = AC d^{\zeta-\varepsilon}, \tag{26}$$

where ε_i is the truncated integer part of ε. Knowing phytoplankton mass and cell numbers, we can solve for parameters A_1 and A_2, and use Eq. (25) instead of (13) for the evaluation of growth as in (15). For a detailed description of the method see Appendix A.

If we do not want to constrain ε to values larger than $\zeta+2$, the integral of Eq. (26) will generally not

converge toward an infinite upper size class. Hence, we compute phytoplankton growth up to a maximum cell size of d_L. To account for growth of cells $>d_L$ we will in the following assume that growth parameters are constant beyond this size.

Growth of the entire community from d_1 to ∞ then is

$$P_{\mathrm{PHY}}(\varepsilon, \mathrm{NO_3}) = V_I A \times \mathrm{NO_3} b_1 \frac{\mu_1}{d_1^2} \times \left[\int_{d_1}^{d_L} \frac{d^{2-\varepsilon}\,\mathrm{d}d}{\frac{K_1}{d_1}d + \mathrm{NO_3}} + \int_{d_L}^{\infty} \frac{d_L^{2-\zeta}\, d^{\zeta-\varepsilon}\,\mathrm{d}d}{\frac{K_1}{d_1}d_L + \mathrm{NO_3}} \right], \quad (27)$$

where the first term inside the brackets is the size-dependent term, and is solved as described above, while the second term describes size-independent growth, and is integrated by standard methods (i.e., without the requirement of integer exponents for d). In the model configuration presented in the next section, d_L is set to a rather high value of 2000 μm. Given a minimum half-saturation constant of $0.005\,\mathrm{mmol\,N\,m^{-3}}$ at a size of 0.2 μm, a cell of 2000 μm would have a half-saturation constant of $50\,\mathrm{mmol\,N\,m^{-3}}$. The model thus explores the approximate range of measured half-saturation constants, from low ($\approx 10^{-3}\,\mathrm{mmol\,N\,m^{-3}}$, Harrison et al., 1996) to high ($>100\,\mathrm{mmol\,N\,m^{-3}}$, Collos et al., 2005) values. To investigate the sensitivity of the model to d_L in Appendix B we present a simulation with an increased upper boundary for size-dependent nutrient uptake ($d_L = 200\,000$ μm), and another one that assumes no growth for cells larger than d_L. The experiments showed very little sensitivity of the model to these changes.

In order to set up the growth term of the phytoplankton cell numbers, we combine the size-dependent nutrient uptake (11) with the assumption that specific nutrient uptake is equivalent to cell divisions. Thereby, we implicitly assume that cells do not change size during their life cycle and that the cell concentration is large enough that we do not have to worry about fractions of a division. As for mass growth, we assume that growth parameters beyond a size d_L do not depend on size. The increase of phytoplankton cell numbers is then defined by

$$P_{\mathrm{NOS}}(\varepsilon, \mathrm{NO_3}) = V_I A \times \mathrm{NO_3} \frac{\mu_1}{d_1^{2-\zeta}} \times \left[\int_{d_1}^{d_L} \frac{d^{2-\varepsilon-\zeta}\,\mathrm{d}d}{\frac{K_1}{d_1}d + \mathrm{NO_3}} + \int_{d_L}^{\infty} \frac{d_L^{2-\zeta}\, d^{-\varepsilon}\,\mathrm{d}d}{\frac{K_1}{d_1}d_L + \mathrm{NO_3}} \right]. \quad (28)$$

Again, analytical solutions for the first integral exist for integer exponents $m = \varepsilon + \zeta - 2$, i.e., with the further restriction of ζ to integer values (in our case: $\zeta = 2$) the first term of the number growth equation can be solved in the same way as Eq. (15). Note that the growth term of the cell numbers contains essentially the same expressions as that of the biomass equation and will therefore not require additional parameterizations or parameters.

To see whether the polynomial approximation of the power-law spectrum (Eq. (25)) has any influence on the model results, we also have investigated a numerical solution to the first terms of Eqs. (27) and (28) which showed little sensitivity of the model to the method of integration (see Appendix B).

Exudation. Below, we solve the integrals for size-dependent phytoplankton mass and particle loss for a variable spectral exponent as determined by Eq. (24). For a variable spectral exponent evaluated according to Eq. (24), we solve the integrals for size-dependent mass and particle loss (Eqs. (29) and (30), respectively). As for the growth term, we assume the loss-rate $\lambda(d)$ to be constant for cells bigger than d_L, and add the corresponding terms. Total mass and number losses due to exudation then are

$$L_{\mathrm{PHY}}(\varepsilon) = AC\lambda_1 d_1 \left[\int_{d_1}^{d_L} d^{\zeta-\varepsilon-1}\,\mathrm{d}d + \int_{d_L}^{\infty} d_L^{-1} d^{\zeta-\varepsilon}\,\mathrm{d}d \right] = \lambda_1\,\mathrm{PHY}\,\frac{\varepsilon - \zeta - 1 + f^{\varepsilon-\zeta}}{\varepsilon - \zeta} \quad (29)$$

for mass and

$$L_{\mathrm{NOS}}(\varepsilon) = A\,\lambda\,d_1 \left[\int_{d_1}^{d_L} d^{-\varepsilon-1} + \int_{d_L}^{\infty} d_L^{-1}\, d^{-\varepsilon}\mathrm{d}d \right] = \lambda_1\,\mathrm{PHY}\,\frac{\varepsilon - 1 + f^{\varepsilon}}{\varepsilon} \quad (30)$$

for cell numbers.

3.4.3. Size-dependent growth in discrete size classes

The most detailed, yet computationally most expensive, way to represent the phytoplankton size distribution is to resolve the size spectrum into a number of individual size classes. In principle, we could assign size-class widths of e.g., 1 μm, i.e., represent the phytoplankton spectrum from 0.2 to 2000 μm by 2000 different size classes, each with its

own set of growth and loss parameters according to their respective cell size. For methodological and practical reasons, size classes are often chosen with logarithmically increasing width, e.g., to the base of 2: 0.2, 0.4, 0.8, 1.6, ... μm for size-class width and/or lower boundary. Here, we follow the latter approach, which reduces the number of size classes required to 14, and includes phytoplankton between 0.2 and 3276 μm. In analogy to empirical methods (see Blanco et al., 1994, for an overview), we assume that mass is distributed evenly within each of these size classes j, i.e., $\varepsilon_j = \zeta = \text{const}$. With this approach, mass of each class can be evaluated according to

$$\mathrm{PHY}_j = \int_{d_j}^{2d_j} A_j C \, \mathrm{d}d = A_j \, C \, d_j. \tag{31}$$

Taking into account the change of growth parameters with size, with $\zeta = 2$ within each discrete size interval, we then evaluate the growth term $P_j(n = 0, \mathrm{NO_3})$ for each class as

$$P_j(n=0,\mathrm{NO_3}) = V_I \, \mathrm{PHY}_j \, \mu_j \frac{\mathrm{NO_3}}{K_j} \ln\left(1 + \frac{1}{1+\frac{\mathrm{NO_3}}{K_j}}\right) \tag{32}$$

with

$$\mu_j = \mu_1 \left(\frac{d_j}{d_1}\right)^{2-\zeta} = \mu_1 \quad \text{and} \quad K_j = K_1 \frac{d_j}{d_1}.$$

Analogously we evaluate the loss by exudation as

$$L_j(\varepsilon = 2) = \mathrm{PHY}_j \, \lambda_j \, \ln(2) = \mathrm{PHY}_j \, \lambda_1 \, \frac{d_1}{d_j} \ln(2). \tag{33}$$

4. Size-dependent growth and exudation in a nutrient–phytoplankton model

We will now investigate the impact of size-dependent processes on the performance of a one-dimensional numerical nutrient–phytoplankton model, which is first run under constant forcing and then under climatological physical forcing that corresponds to a North Atlantic spring bloom site. The model is configured and analyzed according to the following approaches: "constant spectral slope" approach after Hurtt and Armstrong (1999) (NP + HA) and the "variable spectral slope" approach after Kriest and Evans (1999) (NP + KE), 14 discrete phytoplankton size classes (N14P), and no size dependence (NP). In the size-resolving approaches we attempt to account for the entire size range of phytoplankton, i.e., from picophytoplankton (> 0.2 μm diameter) up to giant diatoms such as *Ethmodiscus* sp. (> 1000 μm diameter).

4.1. Model structure and setup

The integral representation of size-dependent phytoplankton growth and exudation introduced above is combined with a simple nutrient–phytoplankton (NP) reaction–diffusion equation. Light limitation is calculated according to Eq. (10), with integration over a day and box thickness as in Evans and Garçon (1997). Phytoplankton production is the product of light- and nutrient-limited growth (cf. Eqs. (20), (27), (32)), instead of the minimum function used by Hurtt and Armstrong (1999) and Kriest and Evans (1999).

$$\frac{\partial \mathrm{NO_3}}{\partial t} = \sum_{j=1}^{j=m} (L_j - P_j + \varepsilon_\mathrm{G} \, \lambda_\mathrm{G} \, \mathrm{PHY}_j) + \frac{\partial}{\partial z} K_z \frac{\partial \mathrm{NO_3}}{\partial z}, \tag{34}$$

$$\frac{\partial \mathrm{PHY}_j}{\partial t} = P_j - L_j - \lambda_\mathrm{G} \, \mathrm{PHY}_j + \frac{\partial}{\partial z} K_z \frac{\partial \mathrm{PHY}_j}{\partial z}, \tag{35}$$

where $m = 1$ for the model configurations NP, NP + HA, and NP + KE, and $m = 14$ for the size-discrete configuration N14P. For the sake of simplicity we parameterized phytoplankton losses due to grazing in the simplest way, i.e., via a linear loss term λ_G, which can be interpreted in two ways: either a saturated zooplankton grazing response, together with the assumption that zooplankton concentration is equal to that of phytoplankton; or zooplankton grazing increasing linearly with phytoplankton concentration, but assuming constant zooplankton concentration. In either case, grazing pressure does not change with phytoplankton size. A fraction ε_G of the grazed phytoplankton biomass is recycled immediately to $\mathrm{NO_3}$; the rest is exported out of the system.

For the size-independent model configuration (NP) we evaluate nutrient uptake by phytoplankton as above, except that growth and loss parameters are kept constant ($\bar{K} = 0.025\,\mathrm{mmol\,N\,m^{-3}}$, $\bar{\lambda} = 0.05\,\mathrm{d^{-1}}$). In this case, $P = V_I \, \mu_1 \, \mathrm{PHY} \, \mathrm{NO_3}/(\bar{K} + \mathrm{NO_3})$ and $L = \bar{\lambda}\,\mathrm{PHY}$ (see Tables 1 and 2). We then present the two size-dependent model configurations NP + HA and NP + KE with parameters

Table 1
State variables, definitions and units of parameters, and parameter values used in the NP model and for the size-dependent approaches

Parameter/state variable	Symbol	Value	Unit
State variables			
Nitrate	NO_3		$mmol\,N\,m^{-3}$
Phytoplankton[a]	$PHY_j,\ j=1,\ldots,m$		$mmol\,N\,m^{-3}$
Number of cells	NOS		$cells\,cm^{-3}$
Biogeochemical parameters			
Max. phytoplankton growth rate	μ_1	2	d^{-1}
Phytoplankton half. sat. constant	K_1, $\bar{K}$	[b]	$mmol\,N\,m^{-3}$
Initial slope of *P–I* curve	α_1	0.05	$(W\,m^{-2}\,d)^{-1}$
Phytoplankton exudation rate	λ_1, $\bar{\lambda}$	[b]	d^{-1}
Phytoplankton mortality	λ_G	0.25	d^{-1}
Recycling efficiency	ε_G	0.50	
Attenuation of light (phytoplankton)	k_{PHY}	0.03	$m^{-1}\ (mmol\,N\,m^{-3})^{-1}$
Attenuation of light (water)	k_w	0.04	m^{-1}
Size parameters			
Minimum cell size	d_1	2×10^{-7}	m
Upper boundary for size dependency	d_L	[b]	m
Minimum cell mass (at size of d_1)	b_1	2×10^{-13}	mmol N
Exponent for cell mass vs. diameter	ζ	2.00	
Exponent of size distribution function	ε	[b]	
Factor of size distribution function	A	[b]	$m^{\varepsilon-4}$

[a]See Table 2 for the number of phytoplankton compartments, m, in the different approaches.
[b]See Table 2 for variation of parameters between the different approaches.

given in Tables 1 and 2. For the size representation in NP + KE with variable spectral exponent ε, we also compute the number of phytoplankton cells (which is needed to compute the exponent ε):

$$\frac{\partial \mathrm{NOS}}{\partial t} = P_{\mathrm{NOS}} - L_{\mathrm{NOS}} - \lambda_G\,\mathrm{NOS} + \frac{\partial}{\partial z} K_z \frac{\partial \mathrm{NOS}}{\partial z}. \quad (36)$$

N14P simulates 14 phytoplankton classes of logarithmically increasing size (base 2, i.e., the diameters, d_j, at the lower boundary of each size class of 0.2, 0.4, 0.8, 1.6, 3.2, 6.4, 12.8, 25.6, 51.2, 102.4 ,204.8, 409.6, 819.2, 1638.4 μm). A further increase in size resolution did not show any significant advances. As for the spectral representations, in the size-discrete approach the half-saturation constant and loss-rate scale with the diameter, d_j, according to Eqs. (32) and (33). Because nitrate appears in the denominator in Eq. (17), all models evaluate nutrient uptake only down to a minimum concentration of nitrate of $10^{-6}\,mmol\,N\,m^{-3}$.

All model configurations are simulated under two different types of physical forcing: first we investigate the effects of constant physical forcing. In this case, the vertical model domain is divided into 40 boxes of 5 m thickness, and the mixing coefficient is set to a low value of $K_z = 0.3\,cm^2\,s^{-1}$ throughout the model domain. Daily integrated photosynthetically available radiation (PAR) at the sea surface is constant ($120\,W\,m^{-2}$), and daylength is 0.5 d. In a

Table 2
Parameters and parameter values used in the different model configurations

Parameter	NP	NP + HA	NP + KE	N14P	Unit
m	1	1	1	14	
A, A_j	–	0.0004[a]	Var.	Var.	$m^{\varepsilon-4}$
ε, ε_j	–	$\zeta+1$	Var.	ζ	
d_L	–	Var.	0.002	0.003276	m
$\bar{\lambda}$, λ_1	0.05	0.20	0.20	0.20	d^{-1}
$\bar{K}$, K_1	0.025	0.005	0.005	0.005	$mmol\,N\,m^{-3}$

Units for parameters as in Table 1. m is the number of phytoplankton compartments.
[a]The value was calculated in the following way: Hurtt and Armstrong (1999) calculated the variation in half-saturation, and the resulting population nutrient uptake analogous to Eq. (20). Combining their model and Eq. (20) with $\beta'_k = 1$, we get $\beta_k = \beta'_k/c = 1/AC$. Hurtt and Armstrong (1999) estimated $\beta_k \approx 5$, resulting in $AC = 0.2\,mmol\,m^{\varepsilon-4-\zeta}$. With $b_1 = 2\times10^{-13}$, $d_1 = 2\times10^{-7}$, $\zeta = 2$, from $b_1 = C\,d_1^{\zeta}$ we find $C = 500\,mmol\,m^{-\zeta}$. Solving for A then gives $A = 1/(5\times500)\,m^{\varepsilon-4} = 0.0004\,m^{\varepsilon-4}$.

second experiment we extended the vertical domain of the model to 400 m depth (40 boxes of 10 m thickness). Monthly mean mixed-layer depths are extracted from Levitus and Boyer (1994) for a site at 48°N 20°W and interpolated by spline interpolation, with a minimum depth given by the thickness of the first box (10 m). Mixing intensity is assumed to be high ($K_z = 300\,\mathrm{cm^2\,s^{-1}}$) in the mixed layer, then gradually decreases within 25 m to a low value ($K_z = 0.3\,\mathrm{cm^2\,s^{-1}}$) at the base of the mixed layer and remains constant for the rest of the model domain (see also Evans and Garçon, 1997). Daily integrated light and daylength for this site were calculated according to Brock (1981).

Lower boundary conditions for nitrate and phytoplankton are set to 10 and $10^{-3}\,\mathrm{mmol\,N\,m^{-3}}$, respectively. We assume "flat" ($\varepsilon = \zeta + 1 = 3$) and nearly "flat" ($\varepsilon = 3.0001$) particle size distributions at the lower model boundary for the NP + HA and NP + KE configuration, respectively. For N14P, the total phytoplankton concentration at the lower model boundary is distributed equally among the 14 phytoplankton groups, again resulting in a flat distribution. Model configurations NP, NP + HA, and N14P are started from $10\,\mathrm{mmol\,N\,m^{-3}}$ nitrate and $10^{-3}\,\mathrm{mmol\,N\,m^{-3}}$ phytoplankton. NP + KE is started with $10\,\mathrm{mmol\,N\,m^{-3}}$ nitrate and $10^{-3}\,\mathrm{mmol\,N\,m^{-3}}$ phytoplankton biomass in the size range of size-dependent growth (i.e., from d_1 to d_L). With an initial distribution determined by $\varepsilon = 3.01$ this results in $0.0114\,\mathrm{mmol\,N\,m^{-3}}$ total phytoplankton (from d_1 to ∞). The model is integrated forward for 7 years, using a variable-coefficient ordinary-differential-equation solver (Brown et al., 1989).

4.2. Results: constant physical forcing

4.2.1. Phytoplankton concentration

The phytoplankton concentration shows a similar response to constant physical forcing under all model configurations: within 10–30 d a bloom develops in the top 40 m, with a maximum concentration of 4–8 $\mathrm{mmol\,N\,m^{-3}}$ (Fig. 2). The bloom peak is very pronounced except for NP + HA. The more moderate bloom development in NP + HA may partly relate to the model's specific assumptions about the size distribution: every increase in mass is accompanied by an increase in the number of large cells, which have a higher half-saturation constant and thus reduce the overall growth rate. The bloom predicted by NP + KE starts later than in N14P, which is not restricted to a certain size distribution and can also produce biomass peaks at a size that is optimal for the given environmental conditions (often in the nanoplankton size range). NP + KE, on the other hand, is bound to a spectral representation of phytoplankton mass, and thus has to account for large or small cells even under conditions that would promote unimodal distributions. For instance, restricting NPKE to the nano- and microphytoplankton size range (2–2000 μm), with a concomitant shift in K_1 and λ_1, strongly increases the similarity between NPKE and N14P (see Fig. 2). The higher effective growth rates simulated by N14P also help to explain the similarity of the bloom simulated by NP and N14P. We note, however, that the parameters ($\overline{K}$ and $\overline{\lambda}$) for NP were chosen more or less arbitrarily, i.e., without any tuning. Choosing a higher $\overline{K}$ would delay the occurrence of the bloom peak, with NP becoming more similar to NP + KE. All model configurations predict the formation of a deep phytoplankton maximum at a depth of about 50–60 m after cessation of the surface bloom, which persists for the rest of the simulation.

4.2.2. Phytoplankton size fractions

Despite similar patterns in total phytoplankton concentration, the size-dependent model configurations differ in how they distribute phytoplankton biomass between different size classes (Fig. 3). In N14P and NP + KE starting from "flat" or almost "flat" phytoplankton size distributions the picophytoplankton (size range 0.2–2.0 μm) initially forms only a small proportion of biomass. During and after the bloom, the contribution of this class increases, until it constitutes almost 100% of total phytoplankton biomass in the upper layers. Nanophytoplankton (2.0–20 μm) plays a role mostly near the surface in the transition toward the oligotrophic system in all size-resolving approaches; in N14P it also contributes considerably to total phytoplankton in deeper layers and in NP + KE below the deep phytoplankton maximum. Microphytoplankton (all cells >20 μm) plays a dominant role in deep water in NP + KE; in N14P it forms between 40% and 60% of the biomass in deeper parts of the model domain. Summarizing, N14P shows a transition from smaller to larger cells in deep parts of the model domain (≈ 160 m), while in NP + KE the transition already appears between 60 and 120 m, with a distinct region of nanophytoplankton in the transition zone.

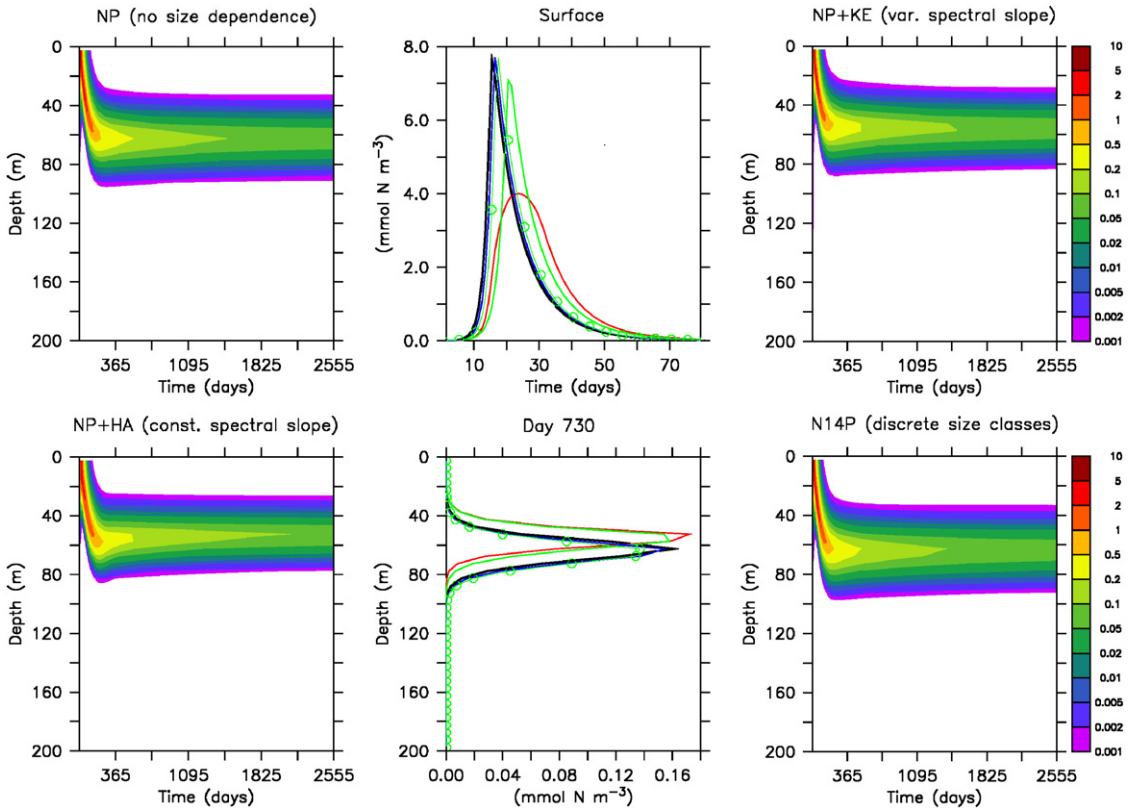

Fig. 2. Phytoplankton concentration (mmol N m^{-3}) under different model configurations, simulated with constant physical forcing. Left and right panels: phytoplankton concentration in the four different model configurations. Upper middle panel: Phytoplankton concentration in the top layer, first 80 days of simulation. Lower middle panel: phytoplankton concentration on day 730. Black line: NP; red line: NP + HA; green line: NP + KE; blue line: N14P. The thin green line with circles denotes an experiment with NPKE, where the size range has been set to 2–2000 μm, with a corresponding shift in λ_1 and K_1.

Total simulated phytoplankton in these deep parts of the model domain is rather low (cf. Fig. 2, and the hatched area in Fig. 3), and from an observing standpoint there would be no detectable phytoplankton, least of all size fractions of phytoplankton. On the other hand, we can detect even very low quantities of phytoplankton in the output of a numerical model; furthermore, the simulated result (greater importance of larger cells in a low-light environment) agrees with the pattern derived theoretically in the previous section. Thus, consistent with the theory N14P and NP + KE suggest that larger phytoplankton is of greater importance in a low-light, eutrophic environment, whereas small phytoplankton dominates mainly the oligotrophic surface layer(s).

NP + HA produces a quite different result: picophytoplankton dominates throughout the vertical model domain and during most of the simulated time, except for the relatively short bloom and transition periods, when nano- and microphytoplankton dominate.

4.2.3. *Trends in simulated size spectra*

In the following we compare the simulated cell size distributions of NP + KE and N14P. NP + KE provides a direct estimate of the exponent of the cell number distribution (13), ε (see Eq. (24)). N14P predicts the biomass PHY_j in the size classes, the distribution within a class given by Eq. (31). We can evaluate the cell number in each class, normalized by its width d_j via

$$\frac{N_j}{d_j} = \mathrm{PHY}_j \frac{1}{b_j d_j} \frac{1 - 2^{1-\zeta}}{\zeta - 1} = \mathrm{PHY}_j \frac{1}{b_j d_j} 0.5, \qquad (37)$$

where b_j is the biomass of a cell at the lower boundary of the class. Assuming an underlying distribution as in Eq. (13), a regression of $\log(N_j/d_j)$ versus $\log(d_j)$ then gives the exponent of the overall

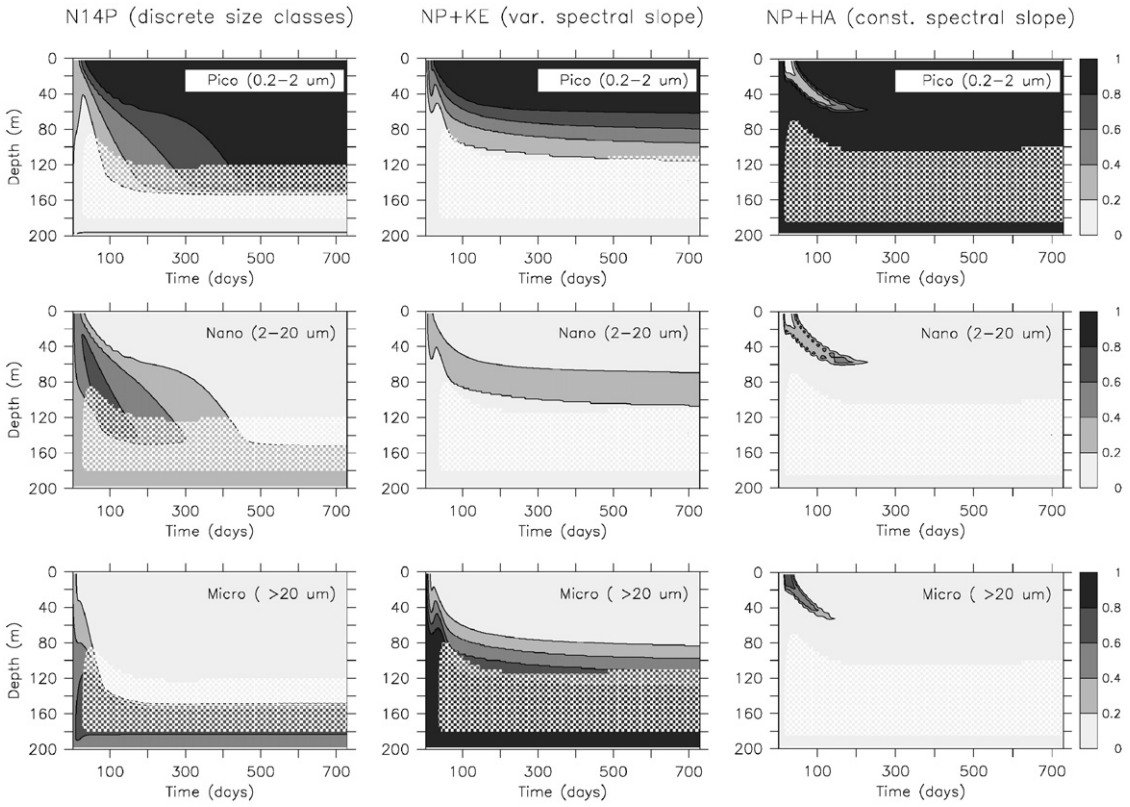

Fig. 3. Fraction of total biomass of three different phytoplankton size classes (0.2–2, 2–20 and $>20\,\mu m$) for the size-dependent model configurations under constant physical forcing, days 1–730. The hatched area indicates regions where total phytoplankton concentration is below 10^{-6} mmol N m^{-3}.

distribution of N14P, ε_D, that can be compared directly to ε of NP + KE. In analogy to in-situ sampling methods, in the regression only size classes with concentrations above a certain threshold (here: $N_j > 10^{-5}$ cells cm^{-3}) are considered.

Starting from essentially "flat" initial distributions, N14P and NP + KE initially mainly show a "rise" of the spectra, and only a small increase of the exponent of the spectrum (Fig. 4 and Table 3), the latter in particular in the first layer. The bloom peak is characterized by a further rise of the spectrum at the surface. When comparing the size distribution of N14P with the exponent predicted by NP + KE we find a slight deviation from linearity (on a log–log scale of normalized cell abundance). The post-bloom period is characterized by rather steep spectra at the surface in both models; the steepness increases strongly during the course of the simulation (day 730). As the simulations approach equilibrium, NP + KE predicts flattening of the size distribution at 60 m depth, while N14P predicts increasing dominance of some picophytoplankton size classes. For these size distribution(s) a linear regression of the log-transformed values at least over the entire size-range does not seem appropriate. At 170 m depth, the model predicts "flat" size distributions (NP + KE) or even increasing biomass in logarithmically increasing size classes (N14P) (Table 3).

Summarizing, a steepening of the size distributions at the surface during the course of the simulation is common to both approaches and is most pronounced for the post-bloom period. Further, both model configurations exhibit a flattening of the size distribution with depth. Both model configurations agree quite well with each other with respect to the estimated exponent (Table 3), except for the deep phytoplankton maximum from the end of year 2, where N14P simulates unimodal size distributions. It is noteworthy that the estimated spectral exponent of N14P is quite sensitive to the minimum cell concentration considered. Consider, for example, the surface size distribution at day 730. If we

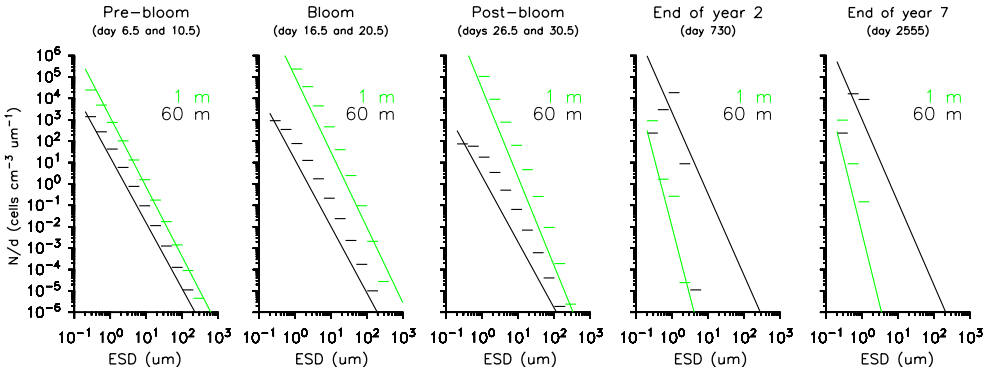

Fig. 4. Number of cells in size class, divided by size-class width, in model configuration N14P and NP + KE simulated with constant physical forcing. Dotted (green) horizontal bars: N14P, 1 m depth. Straight (black) horizontal bars: N14P, 60 m depth. Length of horizontal bars is representative of size-class width. Dotted (green) line: NP + KE, 1 m depth. Straight (black) line: NP + KE, 60 m depth. Results are shown relative to bloom peak (left three panels), after 2 years and after 7 years (two panels on the right). Bloom peak is on day 16.5 in N14P, and on day 20.5 in NP + KE. "Pre-bloom" is 10 d before bloom peak, "post-bloom" is 10 d after bloom peak of the respective model. Normalized cell numbers in each class of N14P have been evaluated as explained in Eq. (37). Normalized cell numbers in each class of NP + KE have been evaluated from the integration of Eq. (13) and divided by size-class width. See also Table 3 for values of the spectral exponents.

Table 3
Exponents of power-law size spectrum for the size-discrete model configuration (ε_D) and for NP + KE (ε) under constant forcing at different times and depths

Depth (m)	Bloom-10		Bloom		Bloom + 10		Day 730		Day 2555	
	ε_D	ε	ε_D	ε	ε_D	ε	ε_D	ε	ε_D	ε
2.5	3.31	3.26	3.87	3.52	4.23	4.12	7.80	6.48	6.34	6.81
57.5	3.12	3.07	3.11	3.11	3.06	3.07	5.71[a]	3.80	−2.61[a]	3.87
167.5	2.91	3.00	2.72	3.00	2.38	3.00	2.34	3.00	2.34	3.00

See Fig. 4 for plots of corresponding size spectra. For the size-discrete model, all regression coefficients r^2 exceed 0.9, except where indicated.

[a]Low regression coefficient ($r^2 = 0.55$ and $r^2 = 0.62$ for days 730 and 2555, respectively). Only size classes with more than 10 cells m^{-3} have been included in the regression for slopes of the size-discrete model configuration.

included only classes with at least 1000 cells m^{-3} (1 cell per liter) the estimated slopes would be smaller (the size distribution "flatter"), because in this case the larger size classes (with few cells) have no influence on the estimated exponent. Further, the increase of cell numbers with size at the lower end of the spectrum (as, e.g., in the deep chlorophyll maximum at the end of the simulation) then plays a larger role. This would be of importance when comparing simulated with observed exponents, and will be discussed in more detail elsewhere.

4.2.4. Variation of community half-saturation constant

The construction of size-dependent model configurations presented in this work was motivated by field observations of variable half-saturation constants of nitrate uptake. To compare the variation of half-saturation constants in the presented model approaches with the observational estimates by Harrison et al. (1996), we have computed a "community half-saturation constant" K^* as follows. Assuming that total phytoplankton production PP is given by

$$\mathrm{PP} = \mathrm{PHY}\, V_I\, \mu_1 \frac{\mathrm{NO_3}}{K^* + \mathrm{NO_3}} \tag{38}$$

and knowing PP, V_I, PHY, NO_3, and μ_1 we can solve for K^* as the half-saturation constant that represents total community growth. K^* is analogous to K_N in Harrison et al. (1996):

$$K^* = \mathrm{NO_3}\left(\frac{V_I\, \mu_1\, \mathrm{PHY}}{\mathrm{PP}} - 1\right). \tag{39}$$

Fig. 5 shows the trajectories of K^* in the surface layer as a function of ambient nitrate concentration, from the start of the simulations ($NO_3 = 10\,mmol\,N\,m^{-3}$) through the bloom and into the stationary phase, when the model adjusts to the deep NO_3 boundary conditions and simulates very low concentrations of NO_3 near the surface. The NP + HA simulation starts with a low phytoplankton concentration ($10^{-3}\,mmol\,N\,m^{-3}$), which in the model context suggests mainly small cells, and so it also starts with low K^*. As phytoplankton concentration increases, more large cells are added and K^* increases quickly. About five days before the peak of the bloom, it has reached its maximum (about $10\,mmol\,N\,m^{-3}$) from which it declines within 10 d by almost two orders of magnitude. At the end of the simulation, phytoplankton concentration and upper size limit for the flat spectrum again are so low that K^* is at its minimum ($0.005\,mmol\,N\,m^{-3}$). The NP + KE simulation starts with a flat spectrum (i.e., large cells dominate the biomass) and an associated large K^* ($\approx 30\,mmol\,N\,m^{-3}$). By the time cells in the size range 0.2–2000 μm start to grow, K^* has already dropped by two orders of magnitude. During the bloom development, nutrient concentrations decrease quickly and so does the proportion of large cells and, as a consequence, K^*.

In principle, the trajectory of K^* in the N14P simulation is quite similar to that of NP + KE, but the initial value (K^* of day 1) of N14P is about an order of magnitude smaller than that of NP + KE, and the decline with decreasing nitrate concentrations is weaker. The smaller initial value of K^* of N14P is caused by the parameterization of the size range, which is finite in N14P, but infinite in NP + KE. Given the flat initial distribution of NP + KE, in this model much biomass is located beyond d_L, i.e., associated with a half-saturation constant of $50\,mmol\,N\,m^{-3}$, which causes the high initial K^* in NP + KE.

In both models, K^* decreases quickly during the first days of simulation; however, 5–10 d before the bloom, K^* of NP + KE still is $>1\,mmol\,N\,m^{-3}$, while K^* of N14P is about an order of magnitude lower. The reason for the lower community half-saturation constant in N14P can be found in its flexible representation of the size distribution, which can select for an optimum size at given environmental conditions, while NP + KE is bound to a spectral representation of the size distribution, from $d_1 - \infty$.

As a consequence, given the rather high K^* and an initial nitrate concentration of $10\,mmol\,N\,m^{-3}$, phytoplankton of NP + KE appears to be nutrient-limited before the bloom, while phytoplankton of N14P can grow with a rate close to its maximum growth rate. This feature may explain the rather late onset of the bloom in NP + KE, and also the similarity between N14P and NP (which has a rather low, fixed value of $\overline{K} = 0.025\,mmol\,N\,m^{-3}$).

4.3. Results: climatological physical forcing

4.3.1. Phytoplankton concentration

As for the constant physical forcing, the phytoplankton concentration develops in a similar way in both the NP and N14P configurations under a climatological forcing scenario. Following the shallowing of the mixed layer, N14P and NP both simulate a phytoplankton spring bloom around day 2350 (in May), and a deep phytoplankton maximum

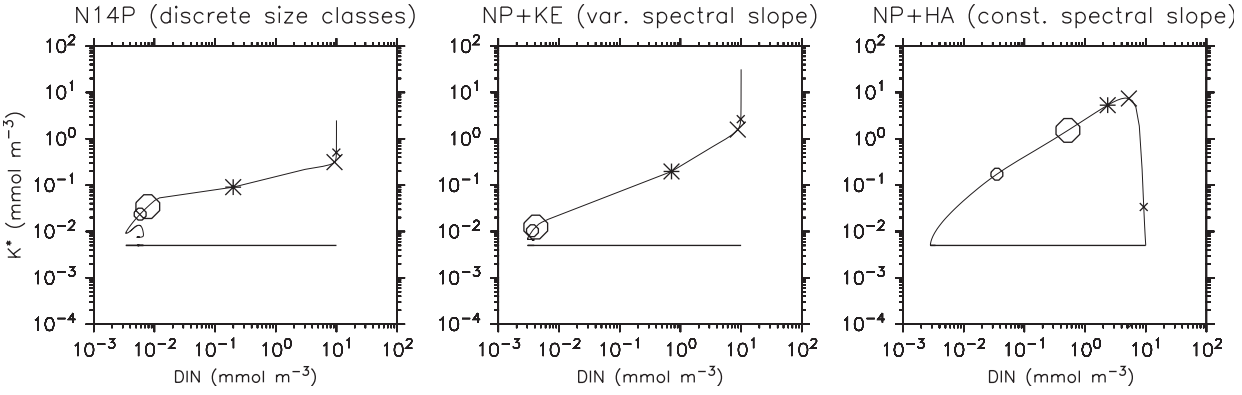

Fig. 5. Trajectory in time of community half-saturation constants K^* for model configurations N14P, NP + KE, and NP + HA in the top layer, constant physical forcing. Symbols indicate different times. Small cross: 10 d before bloom peak. Large cross: 5 d before bloom peak. Asterisk: bloom peak. Large circle: 5 d after bloom peak. Small circle: 10 d after bloom peak. Horizontal line denotes minimum half-saturation constant.

during summer (Fig. 6). In contrast, the spring bloom simulated by NP + HA and NP + KE that parameterize a size spectrum starts about 1 month later, and a deep phytoplankton maximum does not develop in summer. The difference in the development of the phytoplankton concentration between N14P and the spectral model configurations can again be interpreted as a result of the more flexible representation of the size distribution in N14P, which allows cells of optimum size, usually in the nanoplankton size range, to dominate the total phytoplankton community and physiology (see also Section 4.2 for a detailed discussion). As for the simulation with constant forcing, restricting NPKE to the nano- and microphytoplankton size range (2–2000 μm) causes a much earlier bloom, which is similar to the bloom of N14P (see Fig. 6). Again, we note that NP was simulated with more or less arbitrarily chosen parameters, i.e., without any prior tuning; choosing a higher $\overline{K}$ for NP would delay the bloom and increase its similarity to NP + KE.

The rather late onset of the bloom in all model configurations (the simulated North Atlantic station is characterized by a forcing typical for the JGOFS NABE site) is caused mainly by the constantly high grazing pressure in the model during winter (see also Evans and Parslow, 1985). Experiments with different grazing parameterization show that a lower grazing pressure during winter, as simulated by a density-dependent (quadratic) grazing function can indeed produce model results more consistent with observed phytoplankton concentration. Likewise, a non-linear grazing function also produces deep phytoplankton maxima in NP + KE and NP + HA. However, because the focus of this paper is to explore the different nutrient uptake parameterizations, and because the size-resolving model configurations are already non-linear in their

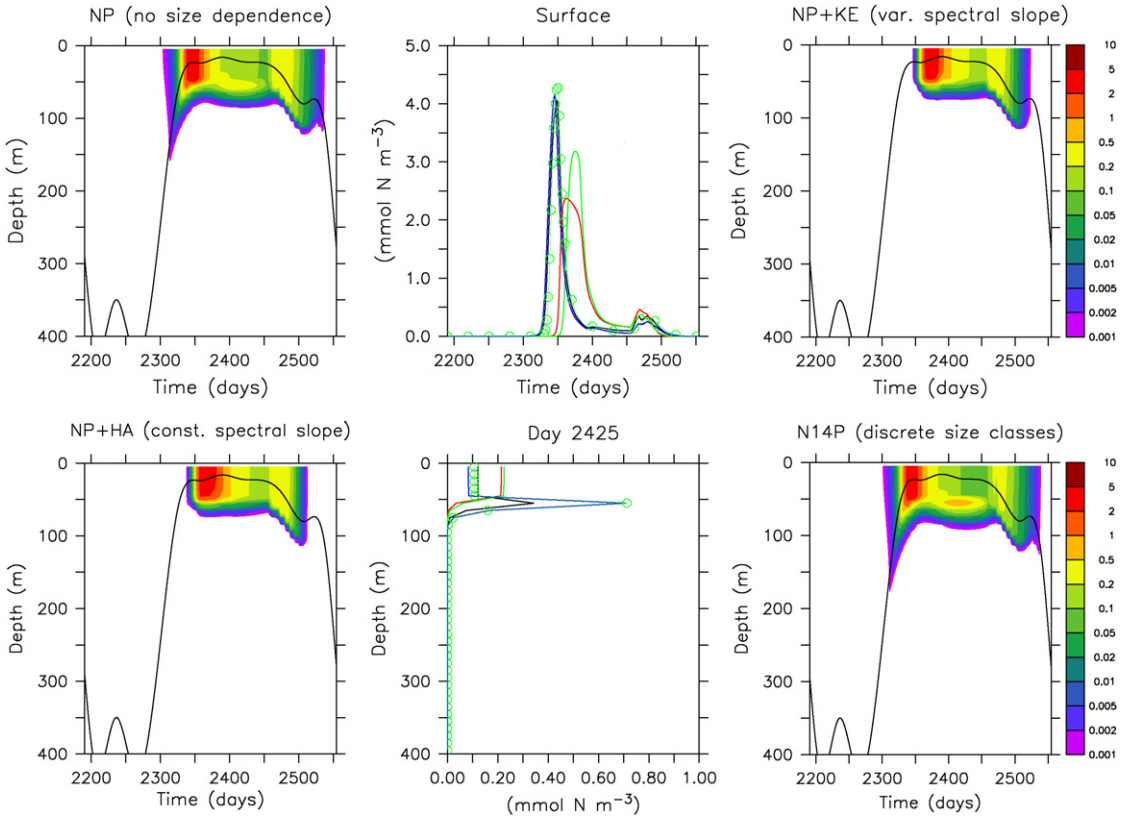

Fig. 6. Phytoplankton concentration (mmol N m^{-3}) under different model configurations in year 7 of simulations forced with climatological annual cycle in mixed-layer depth and solar radiation. Left and right panels: phytoplankton concentration in the four different model configurations. Upper middle panel: phytoplankton concentration in the top layer. Lower middle panel: phytoplankton concentration on day 2425. Black line: NP; red line: NP + HA; green line: NP + KE; blue line: discrete size classes. The thin green line with circles denotes an experiment with NPKE, where the size range has been set to 2–2000 μm, with a corresponding shift in λ_1 and K_1. Line in left and right panels denotes mixed-layer depth (above which $K_z = 300\,\mathrm{cm^2\,s^{-1}}$, see Section 4.1).

nutrient uptake and loss terms, we have decided to restrict all non-linearities to these processes and keep everything else as simple as possible.

4.3.2. Phytoplankton size fractions

Similar to the results obtained with constant physical forcing, NP + KE and N14P in general agree in their prediction of the vertical and temporal distribution of the different size classes (Fig. 7). Picophytoplankton mainly dominates the biomass in the surface layers during summer, while the larger phytoplankton plays a greater role during winter and at moderate to larger depths (note that this is to some extent caused by adjustment to the deep boundary conditions). Nanophytoplankton is of greater importance in the N14P simulation, where it comprises more than 80% of the spring bloom, and more than 60% during spring and at intermediate depths. Microphytoplankton plays a much bigger role in the NP + KE than in the N14P simulation, especially at greater depths.

Note that the relative contribution of each size class to total phytoplankton biomass is governed by the parameters K_1 and λ_1. E.g., a five-fold increase in λ_1, together with a five-fold decrease in K_1 (see Section 2 for possible ranges of these values) will increase the optimum diameter for net growth, and would cause an increase in the relative importance of microphytoplankton in N14P (no figure). Summarizing, consistent with the theory N14P and NP + KE predict an increasing proportion of large phytoplankton biomass with increasing depth, and a dominance of picophytoplankton in the oligotrophic summer system state.

The NP + HA simulation again produces a strikingly different result: owing to its parameterization large cells play a role only during the bloom, while picophytoplankton dominates during the rest of the year, even at greater depths.

4.3.3. Trends in simulated size spectra

The importance of nanophytoplankton in N14P is also reflected in the size distributions, which have been plotted for bloom and non-bloom conditions in Fig. 8. The low-light conditions during winter (day

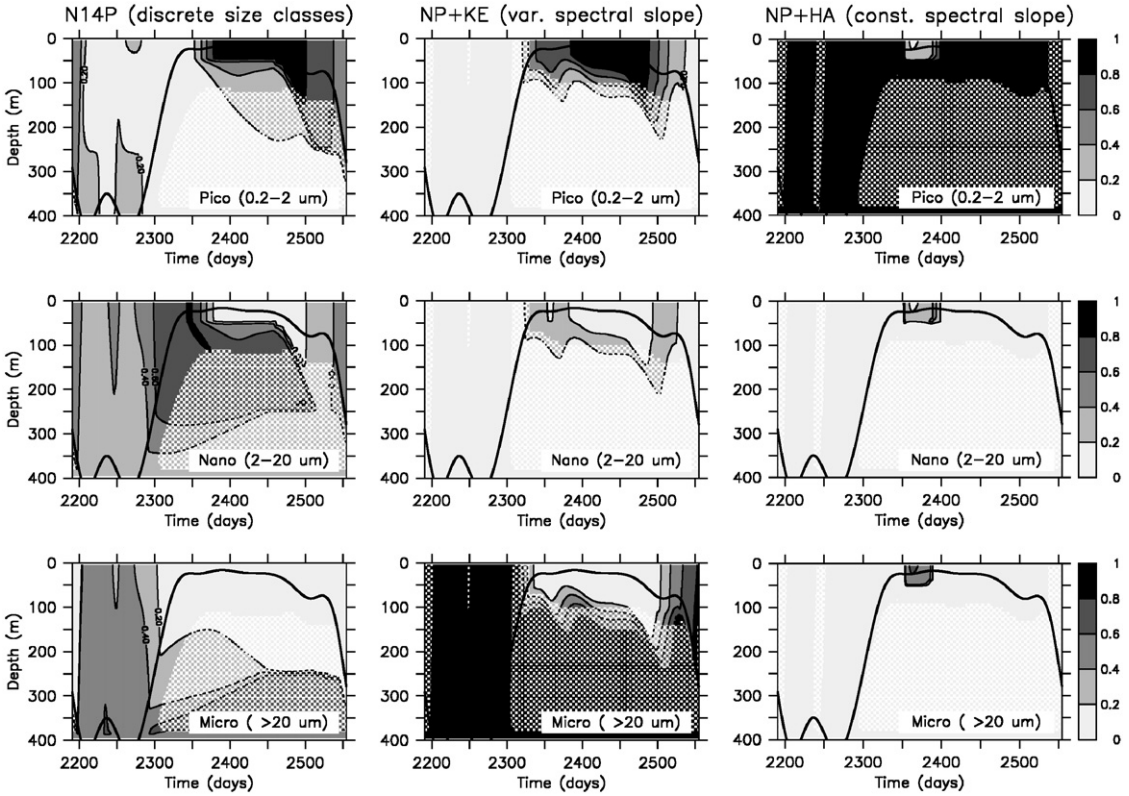

Fig. 7. Fraction of total biomass of three different phytoplankton size classes (0.2–2, 2–20 and $>20\,\mu m$) for the size-dependent model configurations, year 7 of the climatological forcing runs. Solid line denotes mixed-layer depth (above which $K_z = 300\,cm^2\,s^{-1}$). The hatched area indicates regions where total phytoplankton concentration is below 10^{-6} mmol N m^{-3}.

2190, i.e., first day of year 7), together with the deep mixing, provide very unfavorable net growth conditions for the smallest size class (0.2–0.4 μm). This is also reflected in the low regression coefficient of the power-law spectral fit for this time (Table 4). As the mixed layer shallows and light increases toward spring, the contribution of small cells increases. However, the bloom is characterized by a dominance of the 0.8–1.6 μm size class, with the four next larger size classes being also quite abundant. These size classes constitute the peak in nanophytoplankton contribution. The post-bloom period is characterized by rather steep size distributions, especially at the surface. This dominance of the small cells during the oligotrophic summer period affects the composition of the fall bloom, which is initiated by mixed layer deepening and nutrient entrainment. Because of their high abundance during summer, and their low half-saturation constant, small cells also form a major part of this bloom.

Model NP + KE shows a similar development, with rather flat distributions ($\varepsilon \approx 3$) during winter and a steepening of the spectrum as the mixed layer shallows in spring (up to $\varepsilon = 3.57$ on day 2355). The spring bloom is then characterized by a slight decrease in ε to 3.45; the spectrum gets much steeper during the oligotrophic summer period, until the onset of high mixing in fall, which entrains larger cells from below and additionally favors growth of larger cells by lower light and higher nutrients. As for N14P, the fall bloom is characterized by a steeper spectrum ($\varepsilon \approx 4.8$) than the spring bloom.

4.3.4. Variation of community half-saturation constant

Starting with $K^* \approx 0.05\,\mathrm{mmol\,N\,m^{-3}}$ at the beginning of year 7 (small cross in Fig. 9), K^* exhibits a rise in N14P, as mixing entrains larger cells (= "flat" spectra) from the lower model boundary condition, and the environmental conditions at this time of the year additionally promote the growth of large cells. When the mixed layer shallows, K^* decreases to values of about $0.1–0.2\,\mathrm{mmol\,N\,m^{-3}}$ at the height of the bloom, because of the predominant growth of small cells. The summer system is characterized by the dominance of small cells, and consequently, a rather low K^* ($\approx 0.02\,\mathrm{mmol\,N\,m^{-3}}$). The trajectory of K^* therefore resembles that observed in the simulation with constant physical forcing (cf. Fig. 5); however, the way "back" from the oligotrophic summer system state toward the eutrophic winter state with deep mixing shows only a small increase in K^*. The latter is a consequence of the dominance of pico- and nanophytoplankton during late fall and winter down to a depth of about 250 m.

The trajectory of K^* in the NP + KE simulation with climatological forcing also shows similarities to

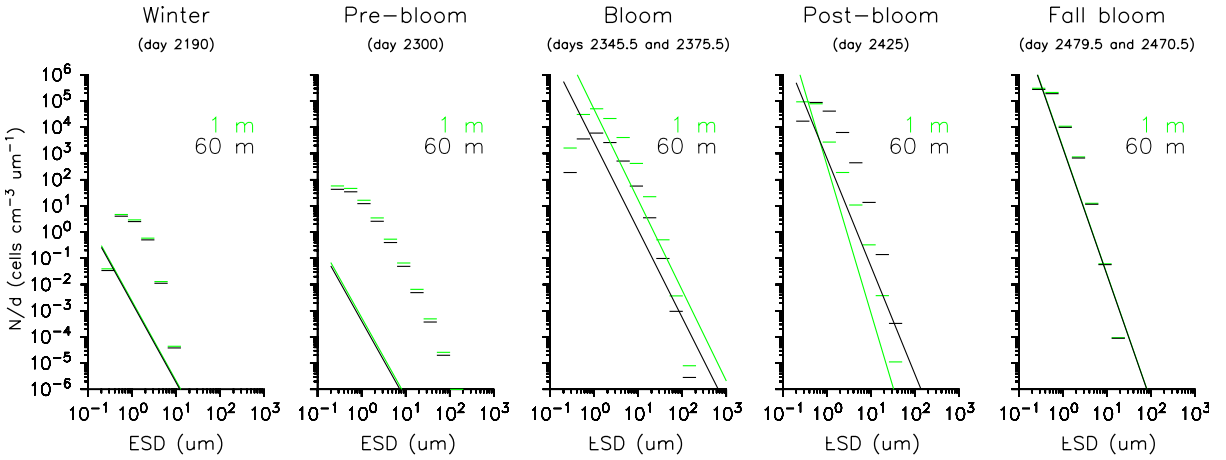

Fig. 8. Number of cells in size class, divided by size-class width, in model configuration N14P and NP + KE simulated with climatological physical forcing. Dotted (green) horizontal bars: N14P, 1 m depth. Straight (black) horizontal bars: N14P, 60 m depth. Length of horizontal bars is representative of size-class width. Dotted (green) line: NP + KE, 1 m depth. Straight (black) line: NP + KE, 60 m depth. Results are shown for winter (day 2190, or first day of year 7), day 2300 (when mixed-layer depth has started to decrease), at spring bloom peak (day 2345 and 2375 for N14P and NP + KE, respectively), during summer (day 2425), and at fall bloom peak (day 2479 and 2470 for N14P and NP + KE, respectively). Normalized cell numbers in each class of N14P have been evaluated as explained in Eq. (37). Normalized cell numbers in each class of NP + KE have been evaluated from the integration of Eq. (13) and divided by size-class width. See also Table 4 for values of the spectral exponents.

Table 4
Exponents of power-law size spectrum for the size-discrete model configuration (ε_D) and for NP + KE (ε) under climatological forcing at different times and depths of year 7

Depth (m)	Day 2190 (1)		Day 2300 (April)		Spring bloom		Day 2425 (Aug)		Fall bloom	
	ε_D	ε	ε_D	ε	ε_D	ε	ε_D	ε	ε_D	ε
2.5	2.20[a]	3.04	2.93	3.00	3.18	3.45	4.71	5.64	5.29	4.84
57.5	2.20[a]	3.04	2.92	3.00	3.02	3.34	3.74	4.12	5.27	4.83
167.5	2.19[a]	3.03	2.88	3.00	0.99[a]	3.00	–[b]	3.02	–[b]	3.03

See Fig. 8 for plots of corresponding size spectra. For the size-discrete model, all regression coefficients r^2 exceed 0.75, except where indicated.

[a]Low regression coefficient.

[b]Too few cells per size class to evaluate the slope of the distribution. Only size classes with more than 10 cells m^{-3} have been included in the regression for slopes of the size-discrete model configuration.

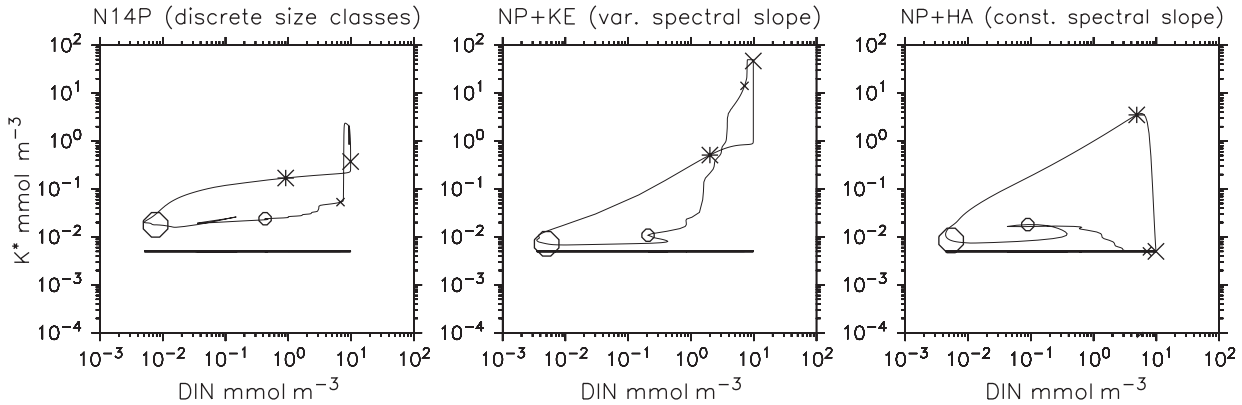

Fig. 9. Trajectory in time of community half-saturation constant K^* for model configurations N14P (size-discrete), NP + KE and NP + HA in the top layer, year 7 of runs with climatological physical forcing. Symbols indicate different times. Small cross: day 2190. Large cross: day 2300. Asterisk: spring bloom peak. Large circle: day 2425. Small circle: fall bloom peak. Horizontal line denotes minimum half-saturation constant.

the simulation with constant forcing; however, the transition from the fall bloom toward the winter system state with high mixing is accompanied by a strong increase in K^*, as a direct consequence of the dominance of large cells, or "flat" size distributions, from about 100 m downwards. The trajectory of K^* in the NP + HA simulation with climatological forcing is also similar to the one with constant forcing. As for N14P the progression from summer to winter exhibits almost no changes in K^*.

5. Discussion

5.1. How realistic is the assumption of a power spectrum?

Both size-spectral model configurations (NP+HA and NP + KE) make very strict assumptions of the particle distribution being representable by a power law, and, in the case of NP + HA, about its parameters. As shown for the size-dependent nutrient uptake and loss-rates in Sections 2 and 3, we cannot, in general, expect a power law to result from these size-dependent processes. Various functions have been used to represent particle size distributions determined from particle abundance (biomass, volume) observed in the field. A power law is often used to describe particle size distributions in the ocean, but other functions have been suggested as well (Zuur and Nyffeler, 1992; Jonasz and Fournier, 1996). Some observations of phytoplankton size spectra indeed suggest deviations from a power law, with biomass peaks, caused by different taxonomic groups, imposed on a linear log–log spectrum (e.g., Gilabert, 2001; Cavender-Bares et al., 2001). Other observations suggest that a

linear log–log spectrum may be appropriate and attribute deviations from linearity to the methodologies applied (Quinones et al., 2003). Gin et al. (1999) neglect the small-particle region of the spectrum and consider only the steadily decreasing large-particle region (above ≈ 0.6–$2\,\mu m$) of the spectrum when estimating power-law exponents.

In the present study, we have tested the validity of the power law approach for mechanistic formulations that represent size-dependent nutrient uptake and loss processes. For fixed environmental conditions and in the absence of grazing, these formulations will generally favor a particular size class (Fig. 1). Our model run N14P which explicitly resolves 14 phytoplankton size classes reveals that a linear log–log spectrum may be a valid approximation of the phytoplankton size spectra during much of the annual cycle. Pronounced deviations are found mainly during the spring bloom, during winter, and in the deep phytoplankton maximum. In these situations, a power law tends to overestimate the concentration of very small ($<2\,\mu m$) cells (Fig. 8). In these cases, an approach similar to that by Gin et al. (1999) (i.e., a cutoff of the spectrum at some lower boundary in the picoplankton size range) may improve the fit of a power law to the simulated size distribution. It thus turns out that our power-law model with variable spectral parameters NP + KE produces a good approximation to the size distribution simulated by the explicit multi-size class model in the size range from ≈ 2–$200\,\mu m$.

5.2. How realistic are the variations of spectral exponents?

In general, values for the exponent of a power law derived from field observations (analogous to our ε) vary from ≈ 2 (Marañón et al., 2004) to ≈ 5 (Cavender-Bares et al., 2001), with an average between 3 and 4. (Note that we have converted the observed exponents, b, which are influenced by the type of dependent and independent variable, to an exponent that can be compared directly to our ε. For example, the exponents observed by Marañón et al. (2004) and Cavender-Bares et al. (2001) are converted via $\varepsilon = 3b + 1$.) Observations suggest either an increase (Gin et al., 1999) or a decrease (Rodriguez and Mullin, 1986; Cermeño et al., 2005) of the exponent with depth. Some increase of the exponent in summer systems has also been observed (Gin et al., 1999; Gilabert, 2001). Unfortunately, winter and deep particle concentrations are usually too low to allow for comparison with models. Further, methodological limitations and artifacts (e.g., sample size and size-class width) may influence the estimate of the spectral exponent from observed particle concentrations (Blanco et al., 1994; Vidondo et al., 1997). Therefore, although N14P and NP + KE simulations in some aspects agree with observed distributions (e.g., Rodriguez and Mullin, 1986; Cermeño et al., 2005; Gilabert, 2001), the comparison of model results with observed variations must be viewed with caution. A more detailed comparison of model results with observed spectra will consider the conversion of slopes of power law spectra calculated from different bases (e.g., diameter, volume), and possible artifacts due to sample size and size-class width, and will be presented elsewhere.

5.3. What are the possible effects of grazing and sinking?

In NP + HA and NP + KE, we assume that processes not yet explicitly accounted for in our simple model (e.g., grazing, sinking) do not select against certain size classes. For example, allometric rules for growth and grazing, in combination with a power-law size distribution, may yield normalized size spectra with a slope of ≈ 3.4–4 (Platt and Denman, 1977), a pattern that has been found in the oligotrophic North Atlantic (Quinones et al., 2003). However, a more detailed representation of zooplankton grazing and its size dependence in numerical models may yield different results, because the combined effects of size-dependent grazing parameters may be strongly non-linear, and further complications may arise if we have to consider omnivory and/or several trophic levels.

All model configurations considered here evaluate the nutrient uptake of phytoplankton cells that move with the water, but not relative to it. However, the latter process may influence the relationship between the half-saturation constant and cell size, as the transport coefficient of nutrients toward the cells originally contains a term for molecular diffusion as well as for motility of cells relative to water (Aksnes and Egge, 1991, their Eq. (8)).

For spherical planktonic cells $<1000\,\mu m$, turbulence is unlikely to play a role in the transport of nutrients toward the cells. However, diatoms, in particular, are not spheres, but exhibit a large variety of forms, from cylinders (e.g., *Coscinodiscus*)

to complicated forms with protuberances (e.g., *Chaetoceros*). The deviation of cell geometry from a spherical shape may increase the nutrient flux into the cell (by an increase of the surface-to-volume ratio), and the flux of nutrients toward the cell, by changes in the flow field in the vicinity of the cell surface (Wolf-Gladrow and Riebesell, 1997). In our model we parameterize a mixed phytoplankton population, which may theoretically consist of a variety of shapes and whose effective shape factor does not change with size. Models that account for different species or cell types should account for different geometric shapes to adequately represent the flux of nutrients toward and into the cell.

In the nano- to microplankton size range the sinking rate increases approximately proportional to the cell diameter, with a healthy cell of $d = 100\,\mu m$ sinking about $5\,m\,d^{-1}$ (Smayda, 1970). However, some phytoplankton cells can regulate their bouyancy, e.g., by changes in cell sap composition (see Smayda, 1970, for an overview). Furthermore, there is a big difference in sinking speed between cells of different physiological status: whereas resting spores and senescent cells may sink very quickly, actively growing cells sink at about an order of magnitude slower, or not at all (Waite et al., 1997). Given its large variation and uncertainty about the sinking speed, especially of large phytoplankton, we opted for neglecting the sinking of cells and the associated changes in nutrient transport toward the cell in this paper.

6. Conclusions

Observations and optimization studies indicate that present NPZD-type models may lack important elements of yet unknown ecological rules of marine ecosystems. Attempts to resolve this issue include strategies to make models more complex, e.g., by resolving an increasing number of distinct phytoplankton groups. This increase in complexity is usually accompanied by an increase in the number of biogeochemical parameters, which may be difficult to constrain. In this study we follow an alternative approach and hypothesize that phytoplankton size, and an associated variation in nutrient uptake and loss parameters, can account for some of the physiological variability of the marine phytoplankton community.

This study explores the effect of size-dependent processes in the framework of a simple nutrient–phytoplankton model in an idealized one-dimensional environment, qualitatively representing a typical annual cycle in the North Atlantic spring bloom region. Theoretical considerations and model configurations with different representations of phytoplankton size distributions allow for a mechanistic prediction of vertical and seasonal differences in the distribution of phytoplankton size classes. Assuming constant zooplankton grazing pressure, theory and the results of an explicit size-discrete model and an implicit size-spectral model predict that the biomass of larger cells—or flat distributions—are more important under low-light and nutrient-replete conditions, but that smaller cells dominate near the surface in oligotrophic, high-light conditions.

In many regimes, the computationally more efficient size-spectral model NP + KE is sufficient to reflect the phytoplankton size distribution of the more detailed multi-size class model N14P. However, especially in the deep phytoplankton maximum a unimodal size distribution rather than the power-law assumption used in NP + KE is more realistic. Comparison with a size-spectral model with fixed spectral slope (NP + HA) shows that a temporal and spatial variation of the spectral slope is of advantage when attempting to simulate a dynamic, size-dependent response of the phytoplankton community to environmental factors.

The comparison with phytoplankton size distributions observed in the field is hampered by the sparsity of data, especially for the winter season. A more detailed and comprehensive analysis of available observations is necessary in order to judge the performance of the models, at least with respect to geographical, vertical, and spring-to-summer variations. The simulated variation of the community half-saturation constant K^*, which cannot be accounted for by a standard NPZD-type model, seems realistic as it roughly agrees with observations made by Harrison et al. (1996).

The size-dependent models presented here are by no means comprehensive—yet they account for important size-dependent physiological processes, and may exhibit a more flexible response to different environmental factors than a simple NP model. The spectral representation NP + KE offers a computationally efficient way to describe variations in size without having to parameterize many distinct phytoplankton groups. Incorporation of size-dependent zooplankton grazing and metabolism is likely to increase the realism of the model. This work is currently underway.

Acknowledgments

We thank the three anonymous reviewers, the editor Michael P. Bacon, and the associate editor Richard Matear for their very constructive comments which helped to improve the manuscript. Financial support of the European Commission via MERSEA IP, contract AIP3-CT-2003-502885, is acknowledged.

Appendix A. Evaluation of A_1, A_2, and growth in NP + KE

To integrate the functions (15) and (28) from some lower boundary, d_1, to an upper boundary, d_L, we first approximate the size distribution by a polynomial as in Eq. (25) and then solve for the coefficients A_1 and A_2 of the polynomial. For phytoplankton up to a size d_L that shows size-dependent growth, the solution of the integrals (22) and (23) from d_1 to d_L is

$$\mathrm{NOS}_{d_L} = A\int_{d_1}^{d_L} d^{-\varepsilon}\,\mathrm{d}d = Aa \tag{A.1}$$

$$= \int_{d_1}^{d_L} A_1 d^{-(\varepsilon_i+1)} + A_2\, d^{-\varepsilon_i}\,\mathrm{d}d \tag{A.2}$$

$$= [A_1 a_1 + A_2 a_2], \tag{A.3}$$

$$\mathrm{PHY}_{d_L} = AC\int_{d_1}^{d_L} d^{\zeta-\varepsilon}\,\mathrm{d}d = ACc \tag{A.4}$$

$$= C\int_{d_1}^{d_L} A_1 d^{\zeta-(\varepsilon_i+1)} + A_2 d^{\zeta-\varepsilon_i}\,\mathrm{d}d \tag{A.5}$$

$$= C[A_1\, c_1 + A_2\, c_2] \tag{A.6}$$

with

$$a = d_1^{1-\varepsilon}\frac{1-f^{\varepsilon-1}}{\varepsilon-1} \quad \text{for } \varepsilon \neq 1 \tag{A.7}$$

$$a_1 = d_1^{-\varepsilon_i}\frac{1-f^{\varepsilon_i}}{\varepsilon_i} \quad \text{for } \varepsilon_i \neq 0 \tag{A.8}$$

$$a_2 = d_1^{1-\varepsilon_i}\frac{1-f^{\varepsilon_i-1}}{\varepsilon_i-1} \quad \text{for } \varepsilon_i \neq 1 \tag{A.9}$$

$$c = d_1^{1+\zeta-\varepsilon}\frac{1-f^{\varepsilon-\zeta-1}}{\varepsilon-\zeta-1} \quad \text{for } \varepsilon \neq \zeta+1 \tag{A.10}$$

$$c_1 = d_1^{\zeta-\varepsilon_i}\frac{1-f^{\varepsilon_i-\zeta}}{\varepsilon_i-\zeta} \quad \text{for } \varepsilon_i \neq \zeta \tag{A.11}$$

$$c_2 = d_1^{1+\zeta-\varepsilon_i}\frac{1-f^{\varepsilon_i-\zeta-1}}{\varepsilon_i-\zeta-1} \quad \text{for } \varepsilon_i \neq \zeta+1 \tag{A.12}$$

and

$$f = \frac{d_1}{d_L}. \tag{A.13}$$

If ε does not satisfy one of the above conditions, the solution for the corresponding term is $-\ln(f)$. Solving for A_1 and A_2, then gives

$$A_1 = \mathrm{NOS}_{d_L}\frac{c_2 - a_2\dfrac{c}{a}}{a_1\, c_2 - a_2\, c_1}, \tag{A.14}$$

$$A_2 = \mathrm{NOS}_{d_L}\frac{a_1\dfrac{c}{a} - c_1}{a_1\, c_2 - a_2\, c_1}. \tag{A.15}$$

If we assume (as in our base scenario) that phytoplankton size range is infinite, we can relate NOS_{d_L} to total numbers via

$$\mathrm{NOS}_{d_L} = \mathrm{NOS}\,(1 - f^{\varepsilon-1}). \tag{A.16}$$

(Note that because ε is always $>\zeta+1$, the logarithmic solution may be required only for c_2.) We then integrate Eqs. (15) and (28), with the size distribution expressed as the sum of integer power terms. The general expression for the integration of mass growth is

$$\begin{aligned} P(n_i, \mathrm{NO_3}) &= V_I A_i b_1 \frac{\mu_1}{d_1^2}\frac{1}{d_1^{n_i-1}}\left[\sum_{i=1}^{n_i-1}\left(\frac{-K_1}{\mathrm{NO_3}}\right)^{i-1}\frac{1}{(n_i-i)}\right. \\ &\quad -\sum_{i=1}^{n_i-1}\left(\frac{-K_1}{\mathrm{NO_3}}\right)^{i-1}\frac{f^{n_i-i}}{(n_i-i)} \\ &\quad \left.-\left(\frac{-K_1}{\mathrm{NO_3}}\right)^{n_i-1}\ln\left(\frac{K_1+\mathrm{NO_3}f}{K_1+\mathrm{NO_3}}\right)\right]. \end{aligned} \tag{A.17}$$

The term can be solved separately for the two integer exponents $n_1 = \varepsilon_i - 1$ and $n_2 = \varepsilon_i - 2$, with the corresponding factors A_1 and A_2. Total mass growth for any given ε is then

$$\begin{aligned} P(\varepsilon, \mathrm{NO_3}) &= P(n_1, \mathrm{NO_3}) + P(n_2, \mathrm{NO_3}) \\ &= P(\varepsilon_i - 1, \mathrm{NO_3}) + P(\varepsilon_i - 2, \mathrm{NO_3}). \end{aligned} \tag{A.18}$$

For cell number growth, analogously we evaluate

$$\begin{aligned} \mathscr{P}(n_i, \mathrm{NO_3}) &= V_I A_i \frac{\mu_1}{d_1^{2-\zeta}}\frac{1}{d_1^{n_i-1}}\left[\sum_{i=1}^{n_i-1}\left(\frac{-K_1}{\mathrm{NO_3}}\right)^{i-1}\frac{1}{(n_i-i)}\right. \end{aligned}$$

$$-\sum_{i=1}^{n_i-1}\left(\frac{-K_1}{NO_3}\right)^{i-1}\frac{f^{n_i-i}}{(n_i-i)} -\left(\frac{-K_1}{NO_3}\right)^{n_i-1}\ln\left(\frac{K_1+NO_3 f}{K_1+NO_3}\right)\Bigg] \quad (A.19)$$

for $n_1=\varepsilon_i+\zeta-1$ and $n_2=\varepsilon_i+\zeta-2$.

Total cell number growth then is

$$\begin{aligned}\mathscr{P}(\varepsilon,NO_3)&=\mathscr{P}(n_1,NO_3)+\mathscr{P}(n_2,NO_3)\\&=\mathscr{P}(\varepsilon_i+\zeta-1,NO_3)\\&\quad+\mathscr{P}(\varepsilon_i+\zeta-2,NO_3).\end{aligned} \quad (A.20)$$

Appendix B. Sensitivity of the model to size range assumptions and nutrient uptake algorithms

The model with variable spectral exponent puts many restrictions upon the representation of phytoplankton growth. In particular, questions to be raised are

(1) How sensitive is the base model NP + KE to variations of the upper boundary d_L of Eq. (15)? To investigate this we increased the upper boundary by a factor of 100 (from 2000 to 200 000 μm). We find that the upper boundary for integration of the growth term has almost no effect on the surface concentration (circles in Fig. 10) except for a delay by 2 days in the onset of the spring bloom. We have also simulated a scenario where there was neither growth nor loss of cells $>d_L=2000\,\mu m$ (crosses in Fig. 10). Again, there was almost no effect on the development of the model bloom, or on the vertical distribution of phytoplankton after 2 years of simulation.

(2) How sensitive is the model with respect to the representation of the size distribution by a polynomial (Eq. (25))? To investigate this, we evaluated Eq. (15) by numerical integration. To assure accuracy and efficiency even over different length scales we first divided the size spectrum into a sequence of logarithmically (base 2) increasing size classes. For each size class we then applied trapezoidal integration, in conjunction with Simpson's rule (Press et al.,

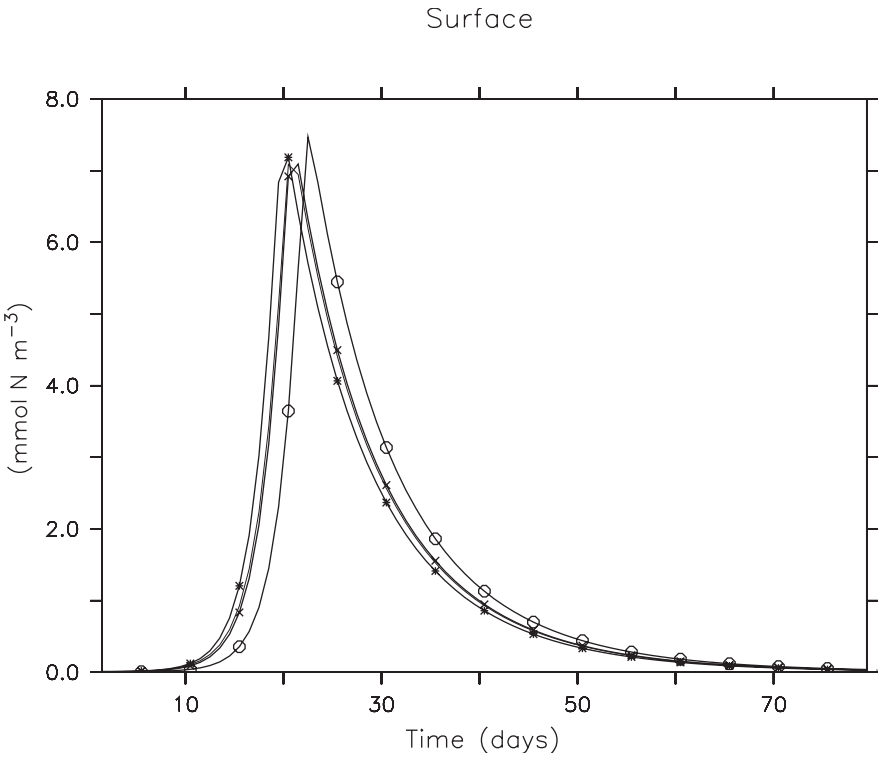

Fig. 10. Experiments with NPKE: phytoplankton concentration in the top layer (mmol N m^{-3}), first 80 days of simulation, simulated with constant physical forcing. Thick black line: standard NPKE. Thin lines with symbols: experiments. Circles: NP + KE with increased upper boundary for integration ($d_L\times 100$). Asterisks: NP + KE with numerical integration of production term P. Crosses: NP + KE, no growth and loss of cells bigger than d_L. See Appendix B for further description of experiments.

1992), up to the desired fractional accuracy of 10^{-3}. However, the simulation with numerical (with respect to size) evaluation of growth shows little differences to the base scenario (Fig. 10).

References

Aksnes, D., Egge, J., 1991. A theoretical model for nutrient uptake in phytoplankton. Marine Ecology Progress Series 70, 65–72.

Baird, M., Oke, P., Suthers, I., Middleton, J., 2004. A plankton population model with biomechanical descriptions of biological processes in an idealized 2D ocean basin. Journal of Marine Systems 50, 199–222.

Banse, K., 1976. Rates of growth, respiration and photosynthesis of unicellular algae as related to cell size—a review. Journal of Phycology 12, 135–140.

Bjørnsen, P.K., 1988. Phytoplankton exudation of organic matter: why do healthy cells do it? Limnology and Oceanography 33 (1), 151–154.

Blanco, J., Echevarría, F., García, C., 1994. Dealing with size-spectra: some conceptual and mathematical problems. Scientia Marina 58 (1–2), 17–29.

Brock, T., 1981. Calculating solar radiation for ecological studies. Ecological Modelling 14, 1–19.

Brown, P.N., Byrne, G.D., Hindmarsh, A.C., 1989. VODE: a variable coefficient ODE solver. SIAM Journal of Scientific and Statistical Computing 10, 1038–1051.

Cavender-Bares, K., Rinaldo, A., Chisholm, S., 2001. Microbial size spectra from natural and enriched ecosystems. Limnology and Oceanography 46 (4), 778–789.

Cermeño, P., Marañón, E., Rodríguez, J., Fernández, E., et al., 2005. Size dependence of coastal phytoplankton photosynthesis under vertical mixing conditions. Journal of Plankton Research 27, 473–483.

Chisholm, S., 1992. Phytoplankton size. In: Falkowski, P., Woodhead, A. (Eds.), Primary Productivity and Biogeochemical Cycles in the Sea. Plenum Press, New York, pp. 213–237.

Collos, Y., Vaquer, A., Souchou, P., 2005. Acclimation of nitrate uptake by phytoplankton to high substrate levels. Journal of Phycology 41, 466–478.

Dadou, I., Evans, G., Garçon, V., 2004. Using JGOFS *in situ* and ocean colour data to compare biogeochemical models and estimate their parameters in the subtropical North Atlantic Ocean. Journal of Marine Research 62, 565–594.

Evans, G., Garçon, V., 1997. One-dimensional models of water column biogeochemistry. JGOFS Report 23, Scientific Committee on Oceanic Research, Bergen, Norway, 85pp. ⟨http://www.scor-int.org/JGOFS/Publications/Report_Series/JGOFS_23.pdf⟩.

Evans, G., Parslow, J., 1985. A model of annual plankton cycles. Biological Oceanography 3, 327–347.

Fasham, M., Evans, G., 1995. The use of optimization techniques to model marine ecosystem dynamics at the JGOFS station at 47°N, 20°W. Philosophical Transactions of the Royal Society of London Series B 348, 203–209.

Fennel, K., Losch, M., Schroeter, J., Wenzel, M., 2001. Testing a marine ecosystem model: sensitivity analysis and parameter optimization. Journal of Marine System 28, 45–63.

Friedrichs, M.A.M., Hood, R., Wiggert, J.D., 2006. Ecosystem model complexity versus physical forcing: quantification of their relative impact with assimilated Arabian Sea data. Deep-Sea Research II 53, 576–600.

Fujiki, T., Taguchi, S., 2002. Variability in chlorophyll a specific absorption coefficient in marine phytoplankton as a function of cell size and irradiance. Journal of Plankton Research 24, 859–874.

Geider, R.J., Platt, T., Raven, J., 1986. Size dependence of growth and photosynthesis in diatoms: a synthesis. Marine Ecology Progress Series 30, 93–104.

Gilabert, J., 2001. Short-term variability of the planktonic size structure in a Mediterranean coastal lagoon. Journal of Plankton Research 23, 219–226.

Gin, K., Chisholm, S., Olson, R., 1999. Seasonal and depth variation in microbial size spectra at the Bermuda Atlantic time series station. Deep-Sea Research I 46, 1221–1245.

Gregg, W., Ginoux, P., Schopf, P., Casey, N., 2003. Phytoplankton and iron: validation of a global three-dimensional ocean biogeochemical model. Deep-Sea Research II 50, 3143–3169.

Harrison, W., Harris, L., Irwin, B., 1996. The kinetics of nitrogen utilization in the oceanic mixed layer: nitrate and ammonium interactions at nanomolar concentrations. Limnology and Oceanography 41 (1), 16–32.

Hurtt, G., Armstrong, R., 1996. A pelagic ecosystem model calibrated with BATS data. Deep-Sea Research II 43 (2/3), 653–683.

Hurtt, G., Armstrong, R., 1999. A pelagic ecosystem model calibrated with BATS and OWSI data. Deep-Sea Research I 46, 27–61.

Jonasz, M., Fournier, G., 1996. Approximation of the size distribution of marine particles by a sum of log-normal functions. Limnology and Oceanography 41 (4), 744–754.

Kriest, I., Evans, G., 1999. Representing phytoplankton aggregates in biogeochemical models. Deep-Sea Research I 46, 1841–1859.

Levitus, S., Boyer, T.P., 1994. World ocean atlas 1994, vol. 4: temperature. In: NOAA Atlas NESDIS 4. U.S. Department of Commerce, Washington, DC. ⟨http://ferret.pmel.noaa.gov/NVODS/servlets/dataset⟩.

Losa, S.N., Kivman, G.A., Ryabchenko, V.A., 2004. Weak constraint parameter estimation for a simple ecosystem model: what can we learn about model and data? Journal of Marine System 45, 1–20.

Marañón, E., Cermeño, P., Rodríguez, J., Zabala, L., et al., 2004. Significance and mechanisms of photosynthetic production of dissolved organic carbon in a coastal eutrophic ecosystem. Limnology and Oceanography 49 (5), 1652–1666.

Matear, R., 1995. Parameter optimization and analysis of ecosystem models using simulated annealing: a case study at station P. Journal of Marine Research 53, 571–607.

McCave, I., 1984. Size spectra and aggregation of suspended particles in the deep ocean. Deep-Sea Research 31 (4), 329–352.

Menden-Deuer, S., Lessard, E., 2000. Carbon to volume relationships for dinoflagellates, diatoms, and other protist plankton. Limnology and Oceanography 45 (3), 569–579.

Montagnes, D., Franklin, D., 2001. Effect of temperature on diatom volume, growth rate, and carbon and nitrogen content: reconsidering some paradigms. Limnology and Oceanography 46 (8), 2008–2018.

Montagnes, D., Berges, J., Harrison, P., Taylor, F., 1994. Estimating carbon, nitrogen, protein and chlorophyll *a* from volume in marine phytoplankton. Limnology and Oceanography 39 (5), 1044–1060.

Mullin, M., Sloan, P.R., Eppley, R.W., 1966. Relationship between carbon content, cell volume, and area in phytoplankton. Limnology and Oceanography 11, 307–311.

Platt, T., Denman, K., 1977. Organization in the pelagic ecosystem. Helgolonder Wissenschaftliche Meeresuntersuchungen 30, 575–581.

Press, W., Teucholsky, S., Vetterling, W., Flannery, B., 1992. Numerical Recipes in C, second ed. Cambridge University Press, Cambridge.

Prunet, P., Minster, J.-F., Ruiz-Pino, D., Dadou, I., 1996a. Assimilation of surface data into a one-dimensional physico-biogeochemical model of the surface ocean: 1. Method and preliminary results. Global Biogeochem. Cycles 10, 111–138.

Prunet, P., Minster, J.-F., Echevin, V., Dadou, I., 1996b. Assimilation of surface data into a one-dimensional physico-biogeochemical model of the surface ocean: 2. Adjusting a simple trophic model to chlorophyll, temperature, nitrate and pCO_2 data. Global Biogeochem. Cycles 10, 139–158.

Quinones, R., Platt, T., Rodriguez, J., 2003. Patterns of biomass-size spectra from oligotrophic waters of the Northwest Atlantic. Progress in Oceanography 57, 405–427.

Raven, J., Kübler, J., 2002. New light on the scaling of metabolic rate with the size of algae. Journal of Phycology 38, 11–16.

Rodriguez, J., Mullin, M., 1986. Relation between biomass and body weight of plankton in a steady state ecosystem. Limnology and Oceanography 31 (2), 361–370.

Schartau, M., Oschlies, A., 2003a. Simultaneous data-based optimization of a 1D-ecosystem model at three locations in the North Atlantic: part I—method and parameter estimates. Journal of Marine Research 61, 765–793.

Schartau, M., Oschlies, A., 2003b. Simultaneous data-based optimization of a 1D-ecosystem model at three locations in the North Atlantic: part II—standing stocks and nitrogen fluxes. Journal of Marine Research 61, 795–821.

Schartau, M., Oschlies, A., Willebrand, J., 2001. Parameter estimates of a zero-dimensional ecosystem model applying the adjoint method. Deep-Sea Research II 48, 1796–1800.

Smayda, T., 1970. The suspension and sinking of phytoplankton in the sea. Oceanography and Marine Biology—Annual Review 8, 353–414.

Smith, E., 1936. Photosynthesis in relation to light and carbon dioxide. Proceedings of the National Academy of Sciences 22, 504–511.

Spitz, Y., Moisan, J., Abbott, M., Richman, J., 1998. Data assimilation and pelagic ecosystem model: parameterizations using time series observations. Journal of Marine System 16, 51–68.

Spitz, Y., Moisan, J., Abbott, M., 2001. Configuring an ecosystem model using data from the Bermuda Atlantic Time Series (BATS). Deep-Sea Research II 48, 1733–1768.

Strathmann, R., 1967. Estimating the organic carbon content of phytoplankton from cell volume or plasma volume. Limnology and Oceanography 12, 411–418.

Taguchi, S., 1976. Relationship between photosynthesis and cell size of marine diatoms. Journal of Phycology 12, 185–189.

Tang, E., 1995. The allometry of algal growth ranges. Journal of Plankton Research 17 (6), 1325–1335.

Vidondo, B., Prairie, Y., Blanco, J., Duarte, C., 1997. Some aspects of the analysis of size spectra in aquatic ecology. Limnology and Oceanography 42 (1), 184–192.

Waite, A., Fisher, A., Thompson, P., Harrison, P., 1997. Sinking rate versus cell volume relationships illuminate sinking rate control mechanisms in marine diatoms. Marine Ecological Progress Series 157, 97–108.

Weilenmann, U., O'Melia, C., Stumm, W., 1989. Particle transport in lakes: models and measurements. Limnology and Oceanography 34 (1), 1–18.

Wolf-Gladrow, D., Riebesell, U., 1997. Diffusion and reactions in the vicinity of plankton: a refined model for inorganic carbon transport. Marine Chemistry 59, 17–34.

Zuur, E., Nyffeler, F., 1992. Theoretical distributions of suspended particles in the ocean and a comparison with observations. Journal of Marine Systems 3, 529–538.